

See discussions, stats, and author profiles for this publication at: <https://www.researchgate.net/publication/235936004>

Multistep Crystallization Process Involving Sequential Formations of Density Fluctuations, “Intermediate Structures”, and Lamellar Crystallites: Poly(3-Hydroxybutyrate) As Investig...

ARTICLE *in* MACROMOLECULES · DECEMBER 2011

Impact Factor: 5.8 · DOI: 10.1021/ma201475t

CITATIONS

14

READS

143

8 AUTHORS, INCLUDING:



Nicolas Spegazzini

Massachusetts Institute of Technology

23 PUBLICATIONS 99 CITATIONS

[SEE PROFILE](#)



Takeji Hashimoto

Kyoto University

516 PUBLICATIONS 16,947 CITATIONS

[SEE PROFILE](#)



Sono Sasaki

Kyoto Institute of Technology

108 PUBLICATIONS 1,384 CITATIONS

[SEE PROFILE](#)



Yukihiro Ozaki

Kwansei Gakuin University

916 PUBLICATIONS 17,719 CITATIONS

[SEE PROFILE](#)

Multistep Crystallization Process Involving Sequential Formations of Density Fluctuations, “Intermediate Structures”, and Lamellar Crystallites: Poly(3-hydroxybutyrate) As Investigated by Time-Resolved Synchrotron SAXS and WAXD

Longhai Guo,[†] Nicolas Spegazzini,[†] Harumi Sato,^{*,†} Takeji Hashimoto,^{†,‡} Hiroyasu Masunaga,[§] Sono Sasaki,^{§,†} Masaki Takata,[§] and Yukihiko Ozaki^{*,†}

[†]Department of Chemistry, School of Science and Technology and Research Center of Environmental Friendly Polymer, Kwansei-Gakuin University, Gakuen 2-1, Sanda, Hyogo 669-1545, Japan

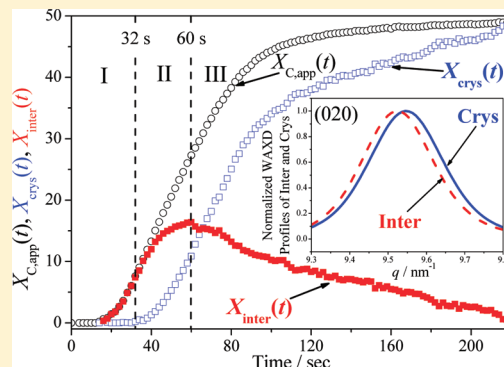
[‡]Professor Emeritus, Kyoto University, Kyoto 606-8501, Japan, and Honorary Chair Professor, National Tsing Hua University, Hsinchu 30013, Taiwan

[§]Japan Synchrotron Radiation Research Institute, 1-1-1, Kouto, Sayo-cho, Sayo-gun, Hyogo 679-5198, Japan

[†]Kyoto Institute of Technology, Matsugasaki, Sakyo-ku, Kyoto 606-8585, Japan

S Supporting Information

ABSTRACT: We explored the isothermal crystallization process of poly(3-hydroxybutyrate) by means of simultaneous measurements of time-resolved wide-angle X-ray diffraction (tr-WAXD) and small-angle X-ray scattering (tr-SAXS) methods. The tr-WAXD analyses involve not only (1) a precise analysis of the integral widths but also the analyses such as (2) two-dimensional correlation spectroscopy (2D-COS) and (3) multivariate curve resolution—alternating least squares (MCR-ALS). The tr-SAXS analyses involve not only (4) the conventional one-dimensional correlation function analysis but also the analyses such as (5) 2D-COS between tr-SAXS and tr-WAXD profiles and (6) 2D-COS of tr-SAXS profiles themselves. These analyses elucidated a multistep crystallization process as classified by region I to III in order of the increasing time. In region I, the density fluctuations are first built up in the amorphous matrix, and then the density-rich regions locally develop “intermediate structures” having the mesomorphic orders between pure amorphous melts and pure crystals [lamellar crystallites (LC)], which then grow into layers of the intermediate structures [defined as mesomorphic layers (ML)] with the long spacings. These results were elucidated by analysis (5) and (6). In region II, LC start to be created from ML, which was elucidated by analysis (1) to (4), and both of the weight fractions of ML (X_{inter}) and LC (X_{crys}) increase with time [analysis (3)]. In region III, X_{inter} and X_{crys} decreases and increases with time, respectively [analysis (3)], because the transformation form ML to LC dominates the transformation from the density fluctuations to ML. The WAXD profiles due to ML in region I was identified by analysis (1), while those in regions II and III were identified by analysis (3).



I. INTRODUCTION

Semicrystalline polymers constitute the largest group of commercially useful polymers, and their crystallization process transforming entangled melts into semicrystalline superstructures has been one of important scientific themes in polymer physics.^{1–3} In this work, we aim to explore the isothermal crystallization process of molten bulk polymers with a particular focus on its early stage, which may involve formation of a various range of mesomorphic orders before formation of well-ordered crystallites, by using simultaneous measurements of time-resolved synchrotron small-angle X-ray scattering (tr-SAXS) and wide-angle X-ray diffraction (tr-WAXD) on a given specimen undergoing crystallization. The polymer to be studied is poly(3-hydroxybutyrate) (PHB),

which is a kind of biodegradable semicrystalline polymer,^{4–9} with orthorhombic crystal structure, $P2_12_1D_2^4$, and lattice parameters $a = 5.76 \text{ \AA}$, $b = 13.2 \text{ \AA}$, and $c = 5.96 \text{ \AA}$ (fiber repeat distance).⁵ The thermal and melting behavior of PHB and PHB-based copolymers and their blends have been investigated by us^{10–17} and several other research groups.^{18,19} An intramolecular hydrogen bonding (HB) $-\text{C}=\text{O}\cdots\text{H}-\text{C}-$ between the $-\text{C}=\text{O}$ group in one helix and one of the $-\text{C}-\text{H}$ group in the $-\text{CH}_3$ group in the other helix along the a -axis has been clarified to stabilize the chain folding in PHB lamellar

Received: June 29, 2011

Revised: October 21, 2011

Published: December 19, 2011

crystallites.^{11–14} The effects of HBs were reported also on the cold crystallization¹⁶ and isothermal crystallization behaviors.^{20,21}

Recently, Zhang et al.²⁰ reported a transient appearance of the IR band around 1731 cm^{-1} with respect to its second derivative spectra during the course of the isothermal crystallization process of PHB and the variation of this band prior to that of the crystalline $-\text{C=O}$ band of PHB (1722 cm^{-1}) by means of the two-dimensional correlation spectroscopy (2D-COS) of the IR bands. Therefore, this 1731 cm^{-1} band was assumed to be due to the “intermediate structures” which are neither pure amorphous melts nor true crystals but rather structures having mesomorphic orders between the melts and the true crystals (well-ordered lamellar crystallites). Suttiwijitpukdee et al.²¹ further reported the transformation of the intermediate structures to the lamellar crystallites without the HBs and then to those with the HBs during the isothermal crystallization process by means of the FTIR analyses. Nevertheless, the structural entity of the intermediate structures was not identified at all in these works. In this work, we define the “intermediate structures” in the same meaning as described above and aim to separate them from the true crystals and identify their diffraction profiles.

The intermediate structures have been generally found for some polymers such as syndiotactic polypropylene (s-PP), isotactic polypropylene (i-PP), polyethylene (PE), poly(ethylene terephthalate) (PET), polycaprolactone (PCL), *cis*-1,4-polybutadiene (PB), etc. Therefore, the identification of them and their WAXD profiles for PHB are quite important to gain deep insights into crystallization from molten polymers in general and to study universality of their existence leading to the well-ordered lamellar crystallites.

Through FTIR study of the isothermal crystallization of PE, Tashiro et al.²² found that the IR band attributed to the mesomorphic phase shows up prior to the appearance of the crystal band. In the early stage of the crystallization process of PE, Kanig²³ reported the existence of intermediate stages during the formation of the lamellar crystallites by means of the transmission electron microscopy with the special staining method. The tr-SAXS and tr-WAXD studies of the isothermal crystallization at varying crystallization temperatures T_c for the cross-linked PB melts drawn by fixed draw ratios λ ^{24,25} revealed that the periodic density fluctuations as observed by the SAXS invariant $Q(t)$ evolve much earlier than the evolution of the crystallinity as observed by tr-WAXD. Moreover, the reports elucidated that the WAXD crystallinity starts to increase with t after the increase of $Q(t)$ with t and that the time lag of the two quantities depends on T_c and λ . This trend was found to be especially remarkable in the case when λ is large and T_c is high. These results may well indicate formation of the intermediate structures prior to formation of the well-developed crystallites, although existence of the intermediate structures was not explicitly mentioned and identified in the reports.^{24,25} Through the investigation of i-PP by time-resolved light scattering, Okada et al.²⁶ and Pogodina et al.²⁷ reported that the development of crystallites occurs much more slowly and appears at much later stages of the crystallization process than that of the density fluctuations. Evolutions of light scattering patterns as well as SAXS profiles preceding the crystallization were also reported by Matsuba et al. for PET.²⁸ Strobl²⁹ proposed the concept of the multistep crystallization process of polymers from melts to homogeneous lamellar crystallites via formation of the following intermediate states: first the mesomorphic layers and then the granular crystalline layers.

Sajkiewicz et al.³⁰ proposed the existence of the intermediate phase in addition to the crystalline and amorphous phases and identified its WAXD profiles during the isothermal and nonisothermal crystallization processes of various PEs by precisely analyzing tr-WAXD profiles.

In this study, we aim to analyze the tr-SAXS and tr-WAXD profiles during the isothermal crystallization process to investigate whether or not PHB develops the density fluctuations and the intermediate structures prior to formation of the lamellar crystallites. If it does, we will try to identify the WAXD profiles attributed to the intermediate structures. The identification of the profiles in turn will stimulate an identification of the corresponding structures. The time variations of SAXS and WAXD profiles are quite similar to those of near-infrared (NIR) and FTIR in the point that the time variations of the various elemental profiles or spectra, which contribute to those of the observed ones, are considerably or heavily superposed each other. It is often difficult to directly decompose the observed profiles or spectra into the elemental ones through the conventional analytical method.

In order to overcome the difficulty described above, we applied the 2D-COS and the multivariate curve resolution–alternating least squares (MCR-ALS) analyses to the tr-WAXD profiles, both of which have widely been used for the analysis of NIR and FTIR spectra with superposed bands. The 2D-COS, proposed by Noda,^{31–33} is a powerful and versatile method for elucidating not only subtle variations of spectra composed of overlapped peaks by spreading the peaks along the second dimension but also a sequential order in the time variation of the elemental spectra induced by an external perturbation such as temperature and time. The MCR-ALS is a powerful tool, which can extract information on the time variation of each of the elemental spectra from the time variation of the observed spectra.^{34–41} These two techniques applied to the tr-WAXD are very ideally suited for investigating the time evolutions of the elemental WAXD profiles, while the 2D-COS between tr-SAXS and tr-WAXD profiles and the 2D-COS of tr-SAXS profiles themselves are useful to investigate the evolutions of the density fluctuations and the intermediate structures, and their sequential order with time, if they exist, as will be detailed in the text. We would like to stress here that precise analyses of the 2D-COS between the tr-SAXS and tr-WAXD and between tr-SAXS themselves enable us to resolve definitely a time difference between evolution of the true crystals via WAXD and that of the long period via SAXS, as will be discussed in section IV-8, although the direct comparisons of the time evolutions between WAXD and SAXS hardly enable us to discern this time difference, as will be elucidated in sections III-2, IV-1, and IV-2.

II. EXPERIMENTAL METHODS

II-1. Materials and Sample Preparation. PHB, which was obtained from the Aldrich Corp., has a number-averaged molecular weight $M_n = 6.5 \times 10^5$, a melting point (T_m) at $175\text{ }^\circ\text{C}$, and a glass transition temperature (T_g) at $0\text{ }^\circ\text{C}$. The sample was hot pressed in a sample holder having its inner diameter of 3 mm and thickness of 0.5 mm at $100\text{ }^\circ\text{C}$ with 5 MPa for 1 min and then rapidly cooled down in air to room temperature. Subsequently, the sample was sealed by a polyimide film on the two sides of the sample holder. The as-prepared sample was used for the measurements of synchrotron radiation SAXS and WAXD.

II-2. Time-Resolved Synchrotron SAXS and WAXD Measurements. The time-resolved SAXS and WAXD experiments were performed in the BL03XU beamline with wavelength $\lambda = 1.0\text{ \AA}$ at

SPring-8, Harima, Japan. The sample-to-detector distances for SAXS and WAXD measurements were set to be 1780 and 60 mm, respectively. The two-dimensional SAXS and WAXD patterns were simultaneously recorded every 2 s with the exposure times of 0.8 and 1 s with a CCD camera (Hamamatsu Photonics, Shizuoka, Japan, V7739P+ORCA R2) and an imaging plate (IP) system (Rigaku, Tokyo, Japan, RAXIS VII), respectively. The SAXS and WAXD profiles were obtained by circularly averaging their two-dimensional patterns as a function of magnitude of the scattering vector, q (0.1–1.7 and 6–27 nm⁻¹, respectively), where $q = (4\pi/\lambda) \sin \theta$, and 2θ is the scattering angle of SAXS or Bragg angle for WAXD, respectively, and λ is wavelength of the incident X-ray beam.

The sample holder was placed in a sample cell made out of copper with a temperature sensor to record the real sample temperature during the experiments. The isothermal crystallization experiments were conducted at 120 °C. For this purpose, a homemade temperature enclosure with two heating chambers (designed hereafter as HC1 and HC2, respectively) was employed for a temperature jump (T -jump) from a temperature above T_m (T_i) to the isothermal crystallization temperature (T_c).⁴² In this experiment, HC1 and HC2 were maintained at $T_i = 180$ °C and $T_c = 120$ °C, respectively. Upon moving synchronously HC1 and HC2 with respect to the sample cell fixed at the center of the incident beam, the sample can be heated by one of these two heating chambers. After 1 min heating of the sample with HC1 to completely erase the thermal history of the sample via melting at T_i , HC1 and HC2 were synchronously moved within 2 s so that HC1 goes out of the sample cell and HC2 comes into the sample cell, and then the sample was controlled at $T_c = 120$ °C with the temperature fluctuation less than ±0.5 °C during the isothermal crystallization process.

II-3. Analysis of WAXD Profiles. The WAXD profiles observed as a function of q and t , $I_{WAXD}^{obs}(q; t)$, during the isothermal crystallization process are composed of the diffraction profiles from “pure amorphous phase” (disordered liquid phase), $I_{WAXD}^{am}(q; t)$, and those from “nonamorphous phase”, $I_{WAXD}^{c,app}(q; t)$, which include the diffraction profiles from not only the lamellar crystallites but also the “intermediate structures” having varying degrees of mesomorphic orders between the pure amorphous phase and crystallites. Hence, $I_{WAXD}^{obs}(q; t)$ is given by

$$I_{WAXD}^{obs}(q; t) = I_{WAXD}^{am}(q; t) + I_{WAXD}^{c,app}(q; t) \quad (1)$$

where $I_{WAXD}^{am}(q; t)$ is obtained in this experiment from the observed profile at 10 s, $I_{WAXD}^{obs}(q; t = 10\text{ s})$, before the onset of the crystallization after the T -jump to T_c . The superscript “ c,app ” in $I_{WAXD}^{c,app}(q; t)$ designates an “apparent crystalline” phase or the nonamorphous phase because it comprises not only the crystallites but also the intermediate structures. In this work, we aim to explore the ordering process of PHB in its early stage of the isothermal crystallization process through the time evolution of $I_{WAXD}^{c,app}(q; t)$.

II-4. Analysis of SAXS Profiles. The time evolution of the characteristic morphological parameters such as average layer thickness of the intermediate structures or the lamellar crystals thickness [$l_c(t)$], average amorphous layer thickness [$l_a(t)$], and average long period [$L(t)$] of the intermediate structures or the lamellar crystals can be evaluated from the one-dimensional correlation function,⁴³ $\gamma(z; t)$, defined by

$$\gamma(z; t) = \int_0^\infty q^2 I_{SAXS,C}(q; t) \cos(qz) dq / Q(t) \quad (2)$$

where z is the direction along which the layer or/and lamellae are stacked with their normals parallel to the z -axis and $Q(t)$ is the scattering invariant

$$Q(t) = \int_0^\infty q^2 I_{SAXS,C}(q; t) dq \quad (3)$$

where $I_{SAXS,C}(q; t)$ is the measured SAXS profiles corrected for the thermal diffuse scattering (TDS), I_{TDS} , to be described below. Since the observed SAXS profiles, $I_{SAXS}(q; t)$, can be collected only over the accessible finite q range, it is necessary to extrapolate them to both high

and low q values for the integration. The extrapolation of the profiles to $q = 0$ is accomplished by using the Guinier law:^{44,45}

$$I_{SAXS}(q; t) = A(t) \exp[-q^2 R_g(t)^2 / 3] \quad (4)$$

where $A(t)$ is a proportionality constant independent of q , and $R_g(t)$ is the radius of gyration of the structural unit relevant to the small q range investigated at time t . The values of $A(t)$ and $R_g(t)$ can be determined through the so-called Guinier plot, $\ln[I_{SAXS}(q; t)]$ vs q^2 , using the intensity data in a sufficiently low q region. The extrapolation of the profiles to the large q can be conducted on the basis of the Porod law:^{46,47}

$$I_{SAXS}(q; t) = I_{TDS} + K_p q^{-4} \quad (5)$$

where K_p is the Porod constant and I_{TDS} is the thermal diffuse scattering which is assumed to be independent of q over the narrow q range covered in this experiment. The values of K_p and I_{TDS} can be determined through the Porod plot, $I_{SAXS}(q; t) q^4$ vs q^4 , using the intensity data in a sufficiently large q region. The I_{TDS} thus evaluated were subtracted from $I_{SAXS}(q; t)$ to obtain $I_{SAXS,C}(q; t)$ and then multiplied by q^2 to correct for the Lorentz factor. The determination of the characteristic parameters (L , l_a , l_c) from the one-dimensional correlation function is shown in detail in Supporting Information 1.

II-5. 2D Correlation Analyses of Time-Resolved WAXD and SAXS Profiles. The Lorentz-corrected SAXS profiles, $q^2 I_{SAXS,C}(q; t)$, as well as the WAXD profiles corrected for the amorphous halo, $I_{WAXD}^{c,app}(q; t)$, taken from 16 s after the induction period, t_0 ($t_0 = 14$ s to be described later in section III in conjunction with Figure 6), during the isothermal crystallization process were selected not only for the homospectral 2D-COS of the WAXD profiles themselves and that of the SAXS profiles themselves but also for the heterospectral 2D-COS between the WAXD and SAXS profiles by using the homemade software. In the synchronous and asynchronous 2D correlation maps, the cross-peaks can be observed with positive or negative intensities. The positive synchronous cross-peak, $\Phi(\nu_1, \nu_2)$, means that the intensity at ν_1 and ν_2 synchronously increases or decreases with time. The negative $\Phi(\nu_1, \nu_2)$ suggests that one of the spectral intensities at ν_1 and ν_2 is increasing with time, while the other is decreasing. When $\Phi(\nu_1, \nu_2)$ is positive, the asynchronous cross-peak, $\Psi(\nu_1, \nu_2)$, becomes positive if the intensity at ν_1 changes before that at ν_2 in the sequential order of time, or $\Psi(\nu_1, \nu_2)$ becomes negative if the intensity at ν_1 changes after that at ν_2 . However, this rule^{31–33} is reversed if $\Phi(\nu_1, \nu_2) < 0$.

II-6. MCR-ALS Analysis of WAXD Profiles. The WAXD profiles, $I_{WAXD}^{c,app}(q; t)$, taken from $t = 16$ to 218 s were selected for the MCR-ALS analysis by using the homemade software. The experimental data $I_{WAXD}^{c,app}(q; t)$ were arranged in a matrix $D = (D_{ij})$ with $i = 1$ to n and $j = 1$ to m , in which $D_{ij} \equiv I_{WAXD}^{c,app}(q_j; t_i)$, so that the j th column represents the time dependence of WAXD intensity at a given q_j and the i th row represents the WAXD intensity profile at a given time t_i . The MCR-ALS analysis allows mathematically the decomposition of the experimental data matrix D into the product of two data matrices C and S^T given as follows

$$D = CS^T + E \quad (6)$$

where the column vector of matrix $C = (C_{ik})$, $C_{ik} = W_k(t_i)$ with $i = 1$ to n and $k = 1$ to l , l being the number of elemental diffraction profiles $I_k(q)$, corresponds to the time dependence of the weight fraction of the k th elemental profile $I_k(q_j)$ with $j = 1$ to m , while the k th row vector of matrix $S^T = (S^T_{kj})$, $S^T_{kj} = I_k(q_j)$ with $k = 1$ to l and $j = 1$ to m , corresponds to the k th elemental diffraction profile, and E is the residual matrix. A more detailed description of this method is provided in Supporting Information 2.

III. RESULTS

III-1. Time-Resolved WAXD. Figure 1a shows some typical WAXD profiles, $I_{WAXD}^{obs}(q; t)$ (black lines), at 10, 30, and 100 s, each of which is vertically shifted relative to the

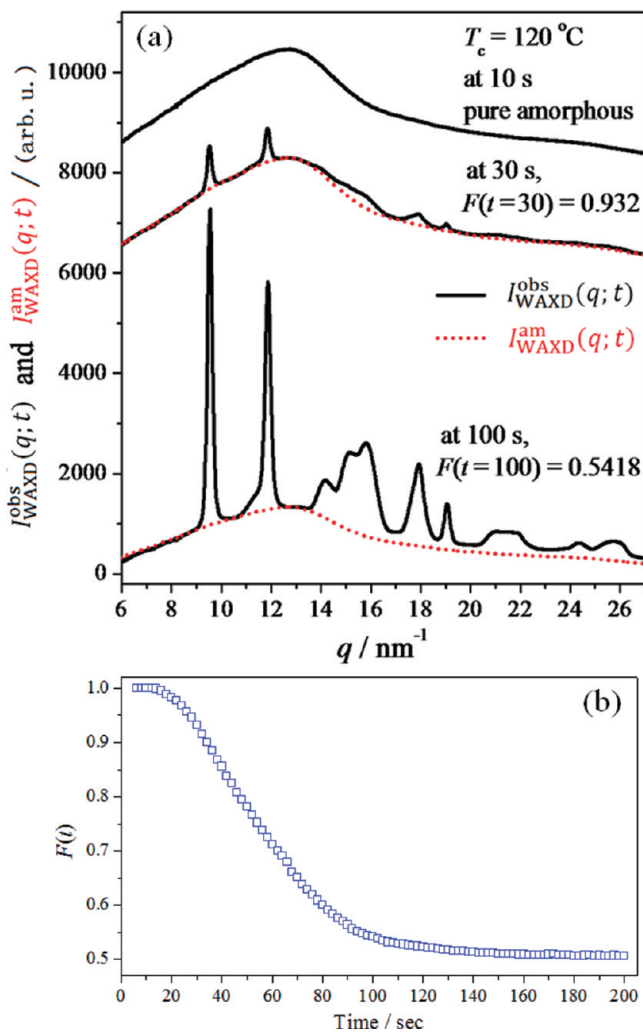


Figure 1. (a) Representative WAXD profiles for PHB observed at 10, 30, and 100 s, $I_{\text{WAXD}}^{\text{obs}}(q; t)$ (black solid lines), and the profiles for the amorphous halos, $I_{\text{WAXD}}^{\text{am}}(q; t)$, at 30 and 100 s (red dotted lines). $I_{\text{WAXD}}^{\text{am}}(q; t)$ was determined from the observed profile $I_{\text{WAXD}}^{\text{obs}}(q; t = 10 \text{ s})$ before the crystallization as follows: $I_{\text{WAXD}}^{\text{am}}(q; t) = F(t)I_{\text{WAXD}}^{\text{obs}}(q; t = 10 \text{ s})$ with $F(t)$ being the reduction factor at time t . (b) $F(t)$ as a function of crystallization time.

bottom profile by the amount of 8000, 6000, and 0 arbitrary units, respectively, to avoid the overlapping of the profiles. Moreover, the figure also displays the best-fitted amorphous halos, $I_{\text{WAXD}}^{\text{am}}(q; t)$ (red dotted lines), together with the factors $F(t)$. $I_{\text{WAXD}}^{\text{am}}(q; t)$ was determined as follows:

$$I_{\text{WAXD}}^{\text{am}}(q; t) = F(t)I_{\text{WAXD}}^{\text{obs}}(q; t = 10 \text{ s}) \quad (7)$$

Here the factor $F(t)$ is defined on the basis of the following concept. The q dependence of the amorphous profile $I_{\text{WAXD}}^{\text{am}}(q; t)$ at a given time t after the isothermal crystallization is equal to that of $I_{\text{WAXD}}^{\text{obs}}(q; t = 10 \text{ s})$ for the observed profile at $t = 10 \text{ s}$ before the onset of crystallization. However, the absolute intensity of $I_{\text{WAXD}}^{\text{am}}(q; t)$ decrease with time t by a factor $F(t)$ because of the conversion of the pure amorphous phase to the nonamorphous phase. The concept introduced here is legitimate without any problems, especially in the early stage where a spatial arrangement of atoms in the amorphous phase hardly changes with time. In this work, we determined $F(t)$ so that $I_{\text{WAXD}}^{\text{obs}}(q; t = 10 \text{ s})$ is best-fitted with the baseline of $I_{\text{WAXD}}^{\text{obs}}(q; t)$, as shown in Figure 1a, and the

factor $F(t)$ thus evaluated as a function of t is shown in Figure 1b. Figure 2 shows the temperature protocol for the T -jump from

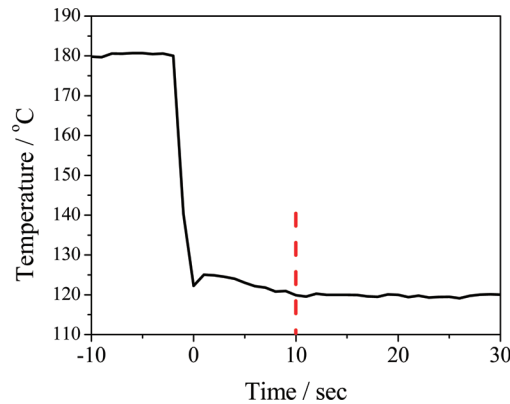


Figure 2. Temperature protocol for the T -jump from 180 to 120 $^\circ\text{C}$.

180 to 120 $^\circ\text{C}$, which was recorded by a sensor embedded in the sample. As shown in the figure, the sample at 10 s has already reached at 120 $^\circ\text{C}$, and local spatial arrangements of atoms in the sample are expected to be equilibrated, judging from the time dependence of the WAXD profile at t around 10 s.

The WAXD profiles of the nonamorphous phase, $I_{\text{WAXD}}^{\text{c,app}}(q; t)$, were obtained by

$$I_{\text{WAXD}}^{\text{c,app}}(q; t) = I_{\text{WAXD}}^{\text{obs}}(q; t) - I_{\text{WAXD}}^{\text{am}}(q; t) \quad (8)$$

The time-resolved profiles from 16 to 200 s are shown in Figure 3 together with the assignment of the lattice plane (hkl)

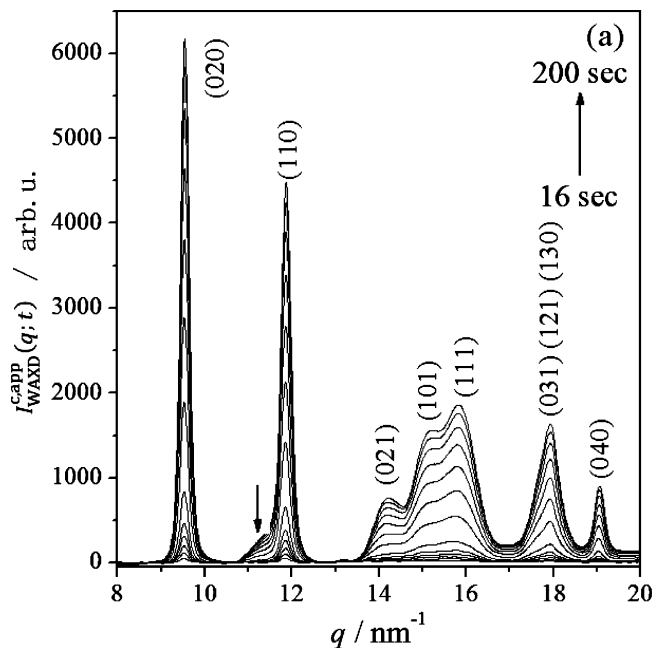


Figure 3. Apparent WAXD diffraction profiles corrected for the amorphous halo, $I_{\text{WAXD}}^{\text{c,app}}(q; t)$.

for each diffraction peak. The profiles in the q regions of 13–17 and 17–18.5 nm^{-1} comprise multiple diffraction peaks. It can be clearly seen from Figure 3 that the areas under the diffraction peaks and their heights increase with time due to the increasing ordering and crystallinity.

The apparent crystallinity $X_{C,\text{app}}(t)$ was calculated from profiles shown in Figures 1 and 3 by using the following equation

$$X_{C,\text{app}}(t) = \frac{\int_{q_{\min}}^{q_{\max}} I_{\text{WAXD}}^{\text{c,app}}(q; t) q^2 dq}{\int_{q_{\min}}^{q_{\max}} I_{\text{WAXD}}^{\text{obs}}(q; t) q^2 dq} \quad (9)$$

where $q_{\min} = 6 \text{ nm}^{-1}$ and $q_{\max} = 27 \text{ nm}^{-1}$. It should be noted that the nonamorphous phase is composed of the intermediate structures with the mesomorphic orders and the lamellar crystallites. Their weight fractions are defined as $X_{\text{int}}(t)$ and $X_{\text{crys}}(t)$, respectively. Thus, $X_{C,\text{app}}(t)$ is a sum of the corresponding two contributions, $X_{\text{int}}(t)$ and $X_{\text{crys}}(t)$, respectively. The result on $X_{C,\text{app}}(t)$ will be discussed later in section IV-1 in conjunction with Figure 6. The integral widths, $\beta_i(t)$, of the diffraction peaks 020 and 110 and the multiple diffraction peaks in the q ranges of 13–17 and 17–18.5 nm^{-1} were calculated from the profiles shown in Figure 3 by using the following equation⁴⁸

$$\beta_i(t) = \frac{\int_{q_{i,\min}}^{q_{i,\max}} I_{\text{WAXD}}^{\text{c,app}}(q; t) q^2 dq}{I_{\text{WAXD}}^{\text{c,app}}(q = q_{p,i}; t) q_{p,i}^2(t)} \quad (10)$$

where i refers to the i th diffraction peak [$i = (020), (110)$, and the two multiple diffraction peaks]; $q_{i,\min}$ and $q_{i,\max}$ denote the limits of the q 's where the i th diffraction intensity for $I_{\text{WAXD}}^{\text{c,app}}$ drops to zero; $q_{p,i}$ is the q value at the i th diffraction peak. As shown in Figure 3, the diffraction peak from the (110) lattice plane is overlapped with the weak diffraction peak as marked by the arrow which exists at $q \approx 11.6 \text{ nm}^{-1}$. The 110 diffraction peak which was separated from the weak diffraction peak was used to evaluate β_{110} . Moreover, the third derivatives of the WAXD profiles were employed to determine the diffraction peak positions of the lattice planes (020) and (110) to calculate lattice parameters $a(t)$ and $b(t)$. The results on $\beta_i(t)$, $a(t)$, and $b(t)$ will be discussed in section IV-2 in conjunction with Figure 8.

III-2. Time-Resolved SAXS. Figure 4a shows time-resolved Lorentz-corrected SAXS profiles during the isothermal crystallization process from 0 to 200 s. Each profile is vertically shifted relatively to its preceding profile with a constant incremental value (0.2 and 0.05 arbitrary units for part a and b, respectively). It is found that a scattering peak appears after some induction period and it increases its intensity and shifts to a large q value with time, which is a common phenomenon observed for isothermal crystallization processes of polymers.^{24,25,49–53} Figure 4b highlights particularly the time evolution of the representative SAXS profiles in the very early stage of the crystallization process from 0 to 36 s, corresponding essentially to time region I defined in section IV-2 in conjunction with Figure 8. It is noteworthy that the SAXS intensity tends to increase, especially at small q regions, even in the time $t < 24 \text{ s}$ before the appearance of clear SAXS peak.

Figure 5 shows some representative one-dimensional correlation functions $\gamma(z; t)$, which were obtained by using eq 2 from the Lorentz-corrected tr-SAXS profiles shown in Figure 4. Through the analysis of the one-dimensional correlation functions, the time evolutions of the characteristic parameters $L(t)$, $l_c(t)$, $l_a(t)$, and Q were obtained, the results of which are shown in Figure 13a, together with the “local apparent crystallinity” $l_c(t)/L(t)$ shown in Figure 13b. Here the

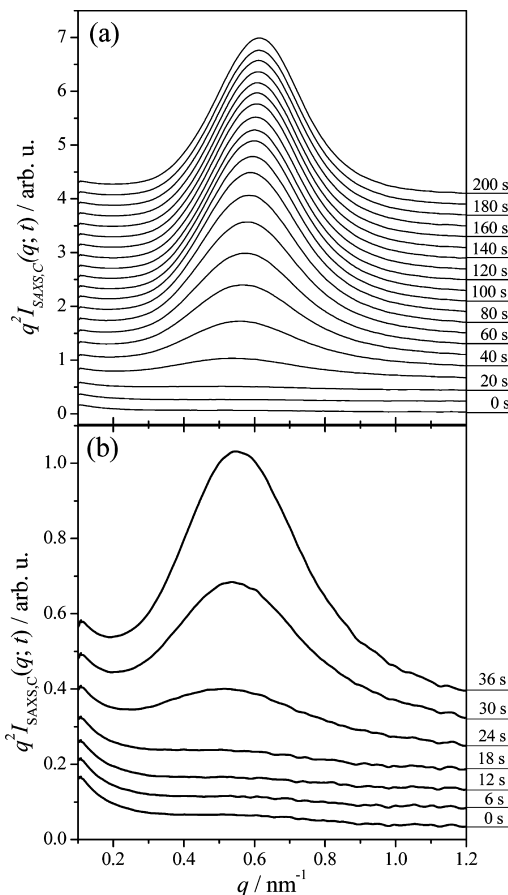


Figure 4. (a) Lorentz-corrected SAXS profiles of PHB obtained during the isothermal crystallization process at 120 °C from 0 to 200 s and (b) from 0 to 36 s. Each profile at a given time is vertically shifted by a constant incremental value [0.2 arbitrary units for (a) and 0.05 arbitrary units for (b)] relative to its preceding profile.

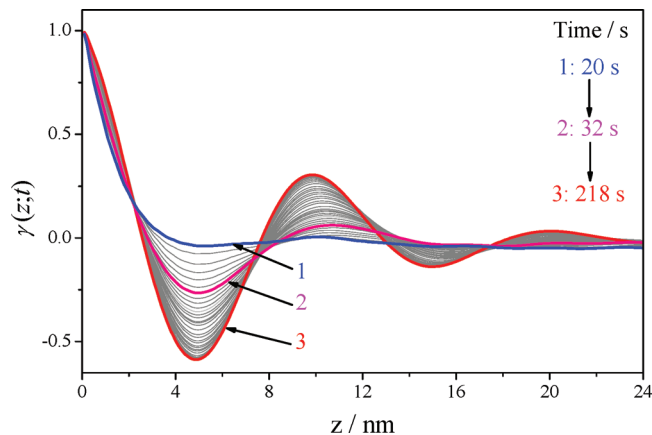


Figure 5. One-dimensional correlation function $\gamma(z; t)$ obtained from the Lorentz-corrected SAXS intensity profiles. The profiles at 20 (blue), 32 (pink), and 218 s (red) are highlighted with thick lines numbered by 1 to 3, respectively.

word “local” is used because the SAXS tends to evaluate apparent crystallinity within grains,^{24,25} when the grains composed of amorphous layers, the mesomorphic layers, and/or the lamellar crystallites are dispersed in the amorphous matrix. The curve 1 at 20 s representative to the early part in region I shows almost a monotonic decrease from 1 to 0 with z ,

which implies the correlation functions characteristic to isolated layers. As time elapses, the correlation function shows an oscillation around zero value with sharper minima and maxima with time, suggesting an increasing order with respect to a periodic arrangement of the mesomorphic layers or/and the lamellar crystallites. The SAXS results will be further analyzed and discussed in sections IV-6 to IV-8 in conjunction with Figures 13 and 14.

IV. ANALYSES AND DISCUSSION

IV-1. Time Evolution of Apparent Crystallinity $X_{C,app}(t)$.

The time evolution of apparent crystallinity $X_{C,app}(t)$ was evaluated by using eq 9, and the result is shown in Figure 6

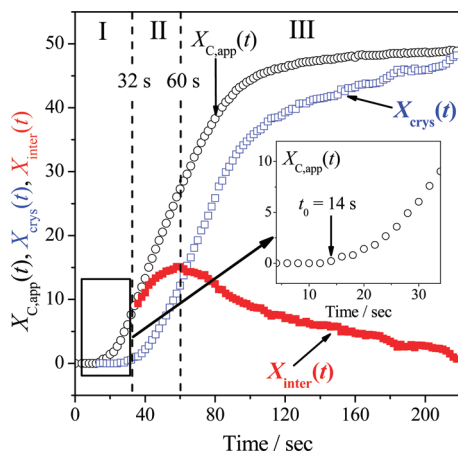


Figure 6. Time-resolved apparent crystallinity, $X_{C,app}(t)$, obtained from the WAXD profiles corrected for the amorphous halo, $X_{inter}(t)$ (the intermediate structures), and $X_{crys}(t)$ (the lamellar crystallites). The inset identifies the induction period $t_0 = 14$ s for the onset of the increasing $X_{C,app}(t)$.

(black symbol) together with $X_{crys}(t)$ and $X_{inter}(t)$. The separation of $X_{C,app}(t)$ into $X_{crys}(t)$ and $X_{int}(t)$ will be discussed later in section IV-4. It can be seen from Figure 6 that $X_{C,app}(t)$ starts to increase from 14 s, indicating that the transformation from pure amorphous phase to the nonamorphous phase starts to occur after the induction period of $t_0 = 14$ s. The figure indicates a classification of the whole time span into the three regions, region I to III, which will be discussed later in conjunctions with Figures 8, 11, and 13.

The evolution of $X_{C,app}(t)$ is sigmoidal with an inflection point around 60 s where the curvature changes from the downward concave curvature to the upward convex curvature. $[\partial X_{C,app}(t)/\partial t]_T$ increases with t in time region I and II and slow down in time region III: It is slowed down especially at $t > 100$ s, seemingly in the secondary crystallization regime in the light of the Avrami plots, $\ln\{-\ln[1 - X_{C,app}(t - t_0)]\}$ vs $\ln(t - t_0)$ and $\ln\{-\ln[1 - X_{crys}(t - t_1)]\}$ vs $\ln(t - t_1)$, where $X_{crys}(t)$ is defined in section IV-4 (eq 12), as indicated in Supporting Information 3.

IV-2. Time Evolution of WAXD Profiles: Elucidation of Multistep Crystallization Process via Intermediate Structures with Mesomorphic Orders. Time-resolved WAXD profiles corrected for the amorphous halo $I_{WAXD}^{C,app}(q; t)$ shown in Figure 3 are enlarged and highlighted around 020 and 110 diffraction peaks in Figure 7a and around the multiple diffraction peaks composed of 021, 101, and 111 in Figure 7b, where we focus on the profiles only up to 100 s, corresponding

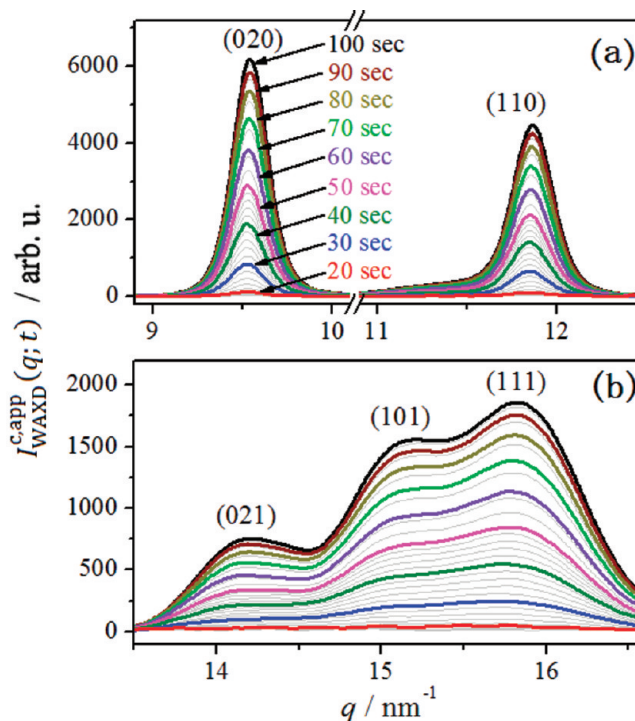


Figure 7. Time-resolved WAXD profiles corrected for the amorphous halo, $I_{WAXD}^{C,app}(q; t)$, in the region of $q = 9–13 \text{ nm}^{-1}$ (a) and $13–17 \text{ nm}^{-1}$ (b) focused on the isothermal crystallization process at 120°C from 16 to 100 s, where the thickened lines are recorded at 20 (red), 30

to roughly the primary stage of the crystallization as inferred from Figure 6. As displayed in the figure, the diffraction peaks are obviously narrowing and becoming intense with time. Figure 8 shows the integral widths of 020 and 110 diffraction peaks, β_{020} and β_{110} , respectively (part a), and the integral widths of the multiple diffraction peak composed of 021, 101, and 111, $\beta_{021,101,111}$, and that composed of 031, 121, and 130, $\beta_{031,121,130}$ (part b), as a function of the crystallization time. The solid lines indicate the integral widths calculated from the MCR-ALS analyses to be discussed later in section IV-4.

The variations of the integral widths with time can be classified into three time regions across the two critical times as indicated by the broken lines around 32 and 60 s. All the integral widths rapidly decrease with time in region I; β_{020} and β_{110} reach a minimum value, while the rates of the decrease of $\beta_{021,101,111}$ and $\beta_{031,121,130}$ with time tend to slow down at the end of region I. In region II, β_{020} and β_{110} increase with time, the rate of which tends to slow down at the end of this region, while the integral widths for the two multiple diffraction peaks keep decreasing with time at the rates much slower than those in region I. All the integral widths remain almost constant at $t > 100$ s in region III.

In order to more clearly investigate the time evolutions of the WAXD profiles in region I, the profiles from 16 to 32 s are more closely investigated with the enlarged Figure 9a, b, in which the profile at 218 s (the black line) is also shown with the intensity reduced by a factor of 0.25 as a reference for the profile relevant to the well crystallized lamellae. It is interesting to note the followings: each of the 020 and 110 diffraction profiles at 218 s has a peak position slightly larger than those up to 32 s. The multiple diffraction profile at 218 s shows the three distinct diffraction peaks around $q = 14.2$, 15.1 , and 15.9 nm^{-1} as shown by the arrows together with the corresponding lattice

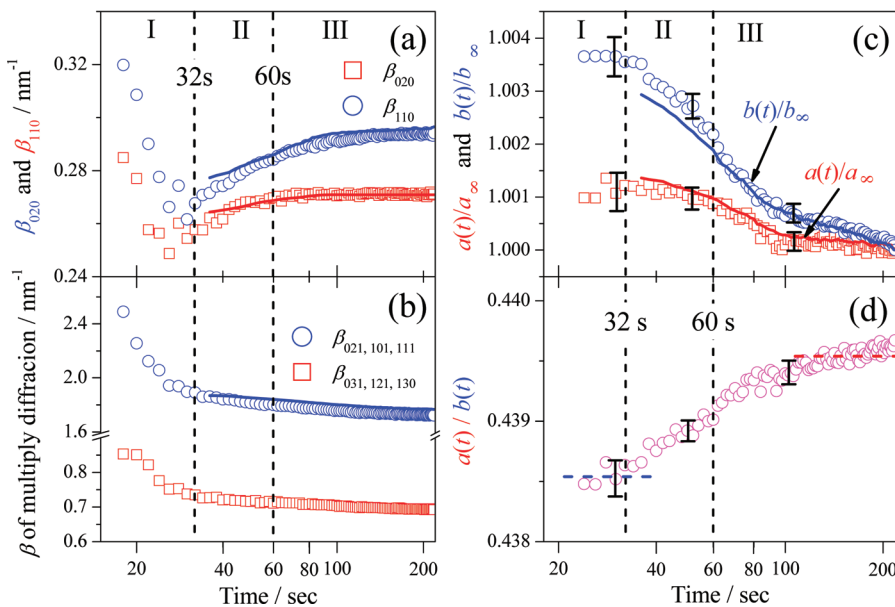


Figure 8. Apparent integral widths of the 020 and 110 diffraction peaks, β_{020} and β_{110} , respectively (a); apparent integral width of the multiple diffraction profile from 021, 101, and 111 peaks, $\beta_{021,101,111}$; that from 031, 121, and 130 peaks, $\beta_{031,121,130}$ (b); the apparent lattice parameters $a(t)$ and $b(t)$ normalized by the respective lattice parameters determined at the long time limit of the crystallization a_∞ and b_∞ (c); the time evolution of the ratio $a(t)/b(t)$ (d). The solid lines were determined from the reconstructed WAXD profiles by using the MCR-ALS analyses.

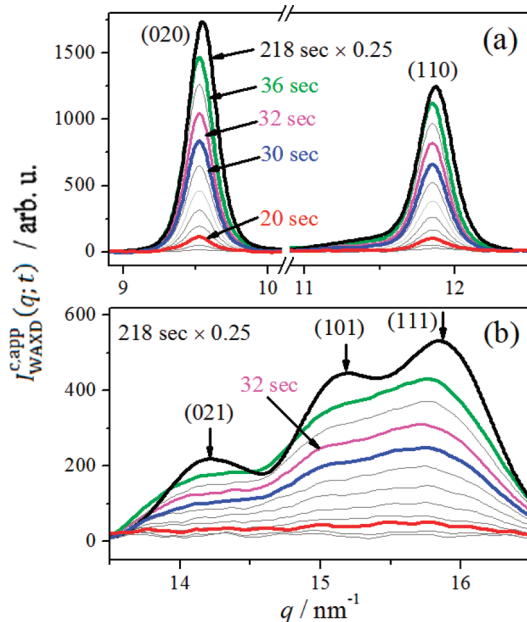


Figure 9. Time-resolved WAXD profiles corrected for the amorphous halo in the region of $q = 9–13 \text{ nm}^{-1}$ (a) and $13–17 \text{ nm}^{-1}$ (b) focused on in the early stage of the isothermal crystallization process from 16 to 32 s (in time region I), where the thick lines are recorded at 20 (red), 30 (blue), 32 (purple), and 36 s (green). The WAXD profile at 218 s (black) with a reduced intensity by a factor of 0.25 is shown as a reference for the profiles from the well-developed crystallites.

planes (021), (101), and (111), respectively, whereas these three diffraction peaks in region I are heavily superposed each other, and only the very broad diffraction peaks, if there are, can be observed at q 's smaller than those at 218 s.

Time Region I. The time evolution of the WAXD profiles in region I may be interpreted on the basis of the following two models: (a) formation of “imperfect crystals” with a large lattice strain or (b) the “intermediate structures” with the

mesomorphic orders. An important question to be addressed here is which model is more plausible: In either case, the decrease of the peak width can be accounted for by the increase of the crystallite size and the lattice perfection in model (a) or by the increase of the intermediate-structure size and the mesomorphic orders in model (b). Thus, both models seem to be feasible on the basis of the WAXD results only. Our previous time-resolved FTIR (tr-FTIR) results on the isothermal crystallization of PHB with a different M_n (2.9×10^5) at a similar temperature (117°C)²¹ provided the following piece of evidence in favor of model (b) as will be described below.

The tr-FTIR showed the evolution of the band at $\sim 1732 \text{ cm}^{-1}$ in the C=O stretching vibration region, which was assigned to be the so-called intermediate structures,²⁰ though details of the structures were left totally unsolved yet. This band was found to appear definitely before the appearance of the crystalline bands at $\sim 1722 \text{ cm}^{-1}$ in the C=O stretching vibration region and at ~ 1229 , ~ 895 , and $\sim 825 \text{ cm}^{-1}$ in the C-H bending and C-O-C stretching vibration region [see Scheme 1 in ref 21]. Moreover, the amorphous bands at ~ 1740 and $\sim 1184 \text{ cm}^{-1}$ were found to decrease their absorbances with time only after the onset of the appearance of the band $\sim 1732 \text{ cm}^{-1}$. These results reveal that there is a time span in which the structures as observed by FTIR are neither pure amorphous states nor crystalline states. If this time span found in tr-FTIR experiments corresponds to region I found in the tr-WAXD experiments, the WAXD profiles in region I is expected to reflect the “intermediate structures” rather the “imperfect crystals”. To further confirm this hypothesis, it is crucial to conduct a simultaneous measurement of tr-WAXD, tr-SAXS, and tr-FTIR. Hereafter, we shall advance our discussion based on model (b). However, the discussion to be developed is valid even in the case when the terminology of the “intermediate structures” is read as that of the “imperfect crystals”.

Those phenomena described above in conjunction with Figures 8 and 9 reveal that, in region I, the isothermal crystallization involves first the transformation of the

amorphous melts into the intermediate structures which have orders between the amorphous melts and the lamellar crystallites. The intermediate structures with the mesomorphic orders give rise to the 020 and 110 diffraction profiles with the larger characteristic spacings and broader widths than those from the well-developed lamellar crystallites formed at 218 s, as shown in Figure 9a. It also gives rise to the multiple diffraction profile with a broader and ill-defined profile than that from the lamellar crystallites at 218 s, as shown in Figure 9b. In Region I, the intermediate structures continuously grow in size and order with time, so that the integral widths keep decreasing, although the characteristic spacings are kept constant.

Time Regions II and III. The increase of β_{020} , β_{110} in region II is due to the onset of the transformation from the mesomorphic orders to the lamellar crystallites with the lattice spacings slightly smaller than those of the mesomorphic orders under such a condition that both the lamellar crystallites and the mesomorphic orders increase in their amount with time. The disparity in the peak positions of these two diffraction profiles and thereby in the respective spacings causes the broadening of the integral widths. In region III, the weight fraction of the lamellar crystallites may further increase at the expense of the mesomorphic orders, thereby giving rise to the almost constant β_{020} and β_{110} or decreasing $\beta_{021,101,111}$ and $\beta_{031,121,130}$. The different time-evolution behavior of the integral widths β_{020} and β_{110} in comparison with that of the multipeaks $\beta_{021,101,111}$ and $\beta_{031,121,130}$ may be due to a heavy overlap of the multipeaks, which may hide the minimum observed in the time evolution of β_{020} and β_{110} at the end of region I. It may depend also on *hkl*-dependent distribution of the mesomorphic orders [in the case of model (b)] or the lattice strain [in the case of model (a)] in the light of the fact that the (020) and (110) lattice planes are parallel to *c*-axis, while the multiple peaks are not.

Figure 8c shows the time evolution of the normalized “apparent lattice parameters” $a(t)/a_\infty$ and $b(t)/b_\infty$ as determined from the diffraction peak positions of the (020) and (110) lattice planes by assuming orthorhombic crystal structure, where a_∞ and b_∞ are the apparent lattice parameters at the long time limit of this experiment (218 s) and those obtained with MCR-ALS analysis (the solid lines) to be discussed later. The spacings $a(t)$ and $b(t)$ in region I are the spacings for the intermediate structures with the mesomorphic orders, while those in region II and III are the weight-averaged spacings between the intermediate structures and the lamellar crystallites. The word “apparent” is used here to note that the spacings are not those only from the well-developed lamellar crystallites themselves. In region I, the apparent spacings $a(t)$ and $b(t)$ of the intermediate structures remain essentially constant with time, while in region II, the apparent spacings are expected to decrease with time because of the onset of formation of the lamellar crystallites with the smaller lattice spacings. The apparent spacings keep decreasing in time region III also because of the increasing amount of the lamellar crystallites with time, though the rate of the decrease tends to slow down at $t > 100$ s in the seemingly secondary crystallization regime, where the hydrogen bondings $-\text{C}=\text{O}\cdots\text{H}-\text{C}-$ between $-\text{C}=\text{O}$ groups and one of $-\text{C}-\text{H}$ groups of $-\text{CH}_3$ of PHB starts to form along the *a*-axis of the lamellar crystallites.^{11,21} Figure 8d presents the time evolution of the ratio $a(t)/b(t)$ again based on the assumption of orthorhombic crystal structure. The ratio is constant in region I as shown by the dashed line within the experimental accuracy, then increases with time in regions II and III, and finally reaches a steady value at the end of region III as also shown by the dashed line.

In order to confirm the above conclusion inferred from the direct analyses of the tr-WAXD profiles, we further conducted the 2D-COS and MCR-ALS analyses on $I_{\text{WAXD}}^{\text{app}}(q; t)$.

IV-3. 2D Correlation Analyses of WAXD Profiles. The crystal structure of PHB is known, and the observed WAXD peaks are related to each other in accordance with the crystal structure. It is needless to say that the 2D correlation analysis to be presented here is based on this basic principle. Within this framework, however, it further adds the following basic information. In the case when the observed diffraction peaks are composed of some elemental peaks which may have different time evolutions, the 2D correlation analysis elucidates in principle existence of the elemental peaks which evolve asynchronously (with time differences) each other.

Consequently, in order to extract more precise and direct pieces of evidence about the evolution of the intermediate structures, we employed the 2D-COS analysis for the time-resolved WAXD profiles corrected for the amorphous halo, which enables one to further explore the time sequences of the evolution of the WAXD profiles due to the intermediate structures and those due to the lamellar crystallites. Figures 10a and 10b display the synchronous 2D correlation maps $\Phi(q_1, q_2)$ and asynchronous 2D correlation map $\Psi(q_1, q_2)$, respectively, generated from the tr-WAXD profiles in the *q* region of 13–17 nm⁻¹ obtained in the time span from 16 to 60 s in time region I and II. Figures 10c and 10d show the three-dimensional display of $\Phi(q_1, q_2)$ and $\Psi(q_1, q_2)$, respectively.

In the synchronous 2D correlation map, three autopeaks are clearly seen to develop around 14.2, 15.2, and 15.9 nm⁻¹ (at positions 1, 2, and 3, respectively) together with positive cross-peaks around (15.9, 15.2), (15.9, 14.2), and (15.2, 14.2) nm⁻¹ (at positions 4, 5, and 6, respectively), indicating that these three diffraction peaks are simultaneously increasing with time. These peak positions are identical to those observed in $I_{\text{WAXD}}^{\text{app}}(q; t)$ at $t = 218$ s [the three arrows on the black line shown in Figure 9b] and expected to be consistent with the PHB orthorhombic crystal structures with the lattice spacings of $a = 5.78$, $b = 13.16$, and $c = 6.027$ Å within the context that the peak positions, and hence the lattice parameters vary with the crystallization conditions. However, in the asynchronous 2D correlation map, in addition to these three diffraction peaks, three diffraction peaks are newly observed remarkably around 13.9, 14.7, and 15.5 nm⁻¹, whose peak positions are smaller than those found in $\Phi(q_1, q_2)$, indicating that the lattice (or apparent lattice) spacings of these three peaks found in $\Psi(q_1, q_2)$ are larger than those observed in $\Phi(q_1, q_2)$. Whether these new peaks can be assigned to the intermediate structures or the imperfect crystals is not clear only from the tr-WAXD results, as discussed in section IV-2. Nevertheless, the 2D synchronous and asynchronous correlation maps unveil the fact that there are at least two kinds of structures relevant to the WAXD profiles developed asynchronously during the isothermal crystallization process: the lamellar crystallites with orthorhombic crystal structure and either the intermediate structures or the imperfect crystals having the apparent lattice spacings larger than the lamellar crystallites. We proposed that the intermediate structures are more plausible than the imperfect crystals with the information obtained from the tr-FTIR as discussed in section IV-2.

If the two diffraction peaks exist in the asynchronous 2D correlation map, the synchronous 2D correlation map should show the cross-peaks between them also. However, the strong overlapping between the two diffraction profiles with the peak

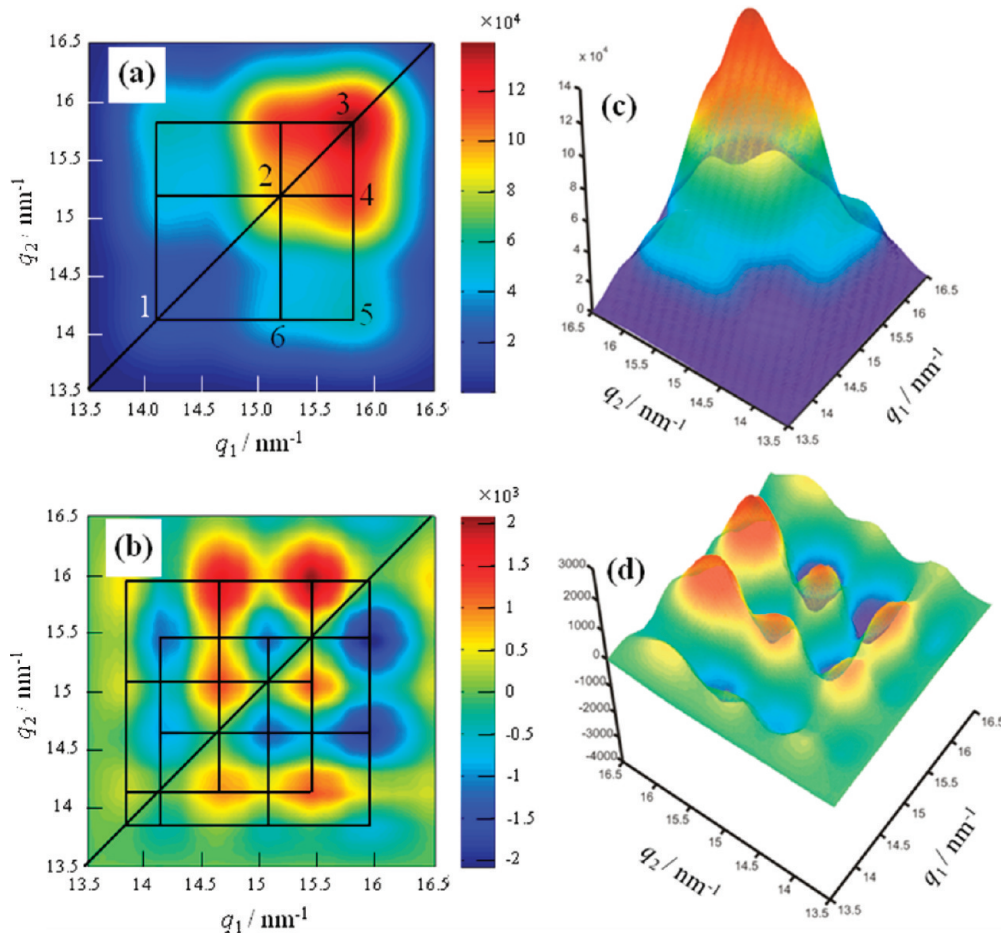


Figure 10. Synchronous (a) and asynchronous (b) 2D correlation maps calculated from the WAXD profiles corrected for the amorphous halo ($13.5\text{--}16.5\text{ nm}^{-1}$) obtained during the isothermal crystallization process (16–60 s) at 120 °C. Parts (c) and (d) show the bird's-eye views of (a) and (b), respectively.

Table 1. Synchronous and Asynchronous 2D Correlation Intensities, $\Phi(k, l)$ and $\Psi(k, l)$, Respectively, with k and l Being the Diffraction-Peak Wavenumber of the Lamellar Crystallites (Denoted L at 14.2, 15.2, 15.9 nm⁻¹) or the Intermediate Structures (Denoted I at 13.9, 14.7, 15.5 nm⁻¹) and the Sequential Order in the Time Variations of the Two Diffraction Peaks at k and l

| no. | $\Phi(k, l)$ | $\Psi(k, l)$ | assign ^a | time sequence |
|-----|------------------------|------------------------|---------------------|------------------|
| 1 | $\Phi(15.9, 13.9) > 0$ | $\Psi(15.9, 13.9) < 0$ | (L, I) | 15.9 after 13.9 |
| 2 | $\Phi(15.9, 14.7) > 0$ | $\Psi(15.9, 14.7) < 0$ | (L, I) | 15.9 after 14.7 |
| 3 | $\Phi(15.9, 15.5) > 0$ | $\Psi(15.9, 15.5) < 0$ | (L, I) | 15.9 after 15.5 |
| 4 | $\Phi(15.5, 14.2) > 0$ | $\Psi(15.5, 14.2) > 0$ | (I, L) | 15.5 before 14.2 |
| 5 | $\Phi(15.5, 15.2) > 0$ | $\Psi(15.5, 15.2) > 0$ | (I, L) | 15.5 before 15.2 |
| 6 | $\Phi(15.2, 13.9) > 0$ | $\Psi(15.2, 13.9) < 0$ | (L, I) | 15.2 after 13.9 |
| 7 | $\Phi(15.2, 14.7) > 0$ | $\Psi(15.2, 14.7) < 0$ | (L, I) | 15.2 after 14.7 |
| 8 | $\Phi(14.7, 14.2) > 0$ | $\Psi(14.7, 14.2) > 0$ | (I, L) | 14.7 before 14.2 |
| 9 | $\Phi(14.2, 13.9) > 0$ | $\Psi(14.2, 13.9) < 0$ | (L, I) | 14.2 after 13.9 |

^aL and I designate the lamellar crystallites and the intermediate structures with the mesomorphic orders.

intensities at the small q values being much weak than those at the large q values makes the synchronous 2D correlation map hardly distinguish the cross-peaks arising from these two structures. Table 1 summarizes signs of various cross-correlation peaks which are expected to exist in the synchronous map $\Phi(k, l)$ and which are actually observed clearly to exist in the asynchronous map $\Psi(k, l)$ with k and l being the diffraction peak positions belonging to either the lamellar crystallites or the intermediate structures, designated as L or I, respectively. According to the Noda's rule³³ in the 2D correlation analysis, the case of $\Phi(k, l) > 0$ and $\Psi(k, l) < 0$ suggests that the l th diffraction peak appears prior to the k th diffraction

peak, while the case of $\Phi(k, l) > 0$ and $\Psi(k, l) > 0$ suggests that the k th diffraction peak appears prior to the l th diffraction peak. According to this rule, the cross-correlation peaks no. 1 in Table 1, which satisfies $\Phi(15.9, 13.9) > 0$ and $\Psi(15.9, 13.9) < 0$, suggest that the peak at $q = 13.9\text{ nm}^{-1}$ appears prior to the peak at $q = 15.9\text{ nm}^{-1}$, thereby the intermediate structures (I) appear prior to the lamellar crystallites (L). All the cross-correlation peaks of Φ and Ψ labeled no. 1 to 9 consistently elucidate that, after the induction period, the intermediate structures develop prior to the lamellar crystallites, which is physically reasonable and supports the validity of the Noda's rule in this case.

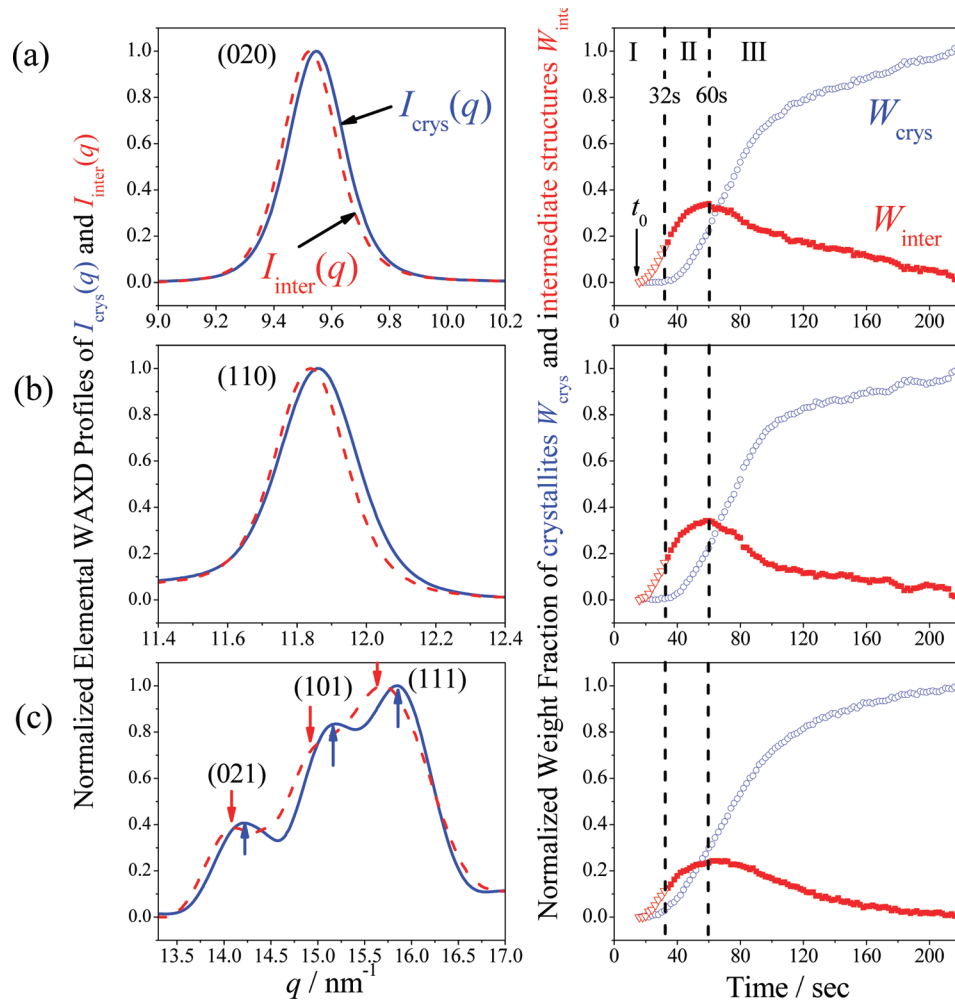


Figure 11. Decomposed elemental WAXD profiles for the intermediate structures [the red dotted lines, $I_{\text{inter}}(q)$] and the lamellar crystallites [the blue solid lines, $I_{\text{crys}}(q)$] (left half) and time evolution of the weight fractions of the intermediate structures (red filled symbols, W_{inter}) and lamellar crystallites (blue unfilled symbols, W_{crys}) in time region II and III during the isothermal crystallization process as determined by the application of MCR-ALS to the following observed profiles: (a) 020; (b) 110; (c) the multiple diffraction peaks composed of 021, 101, and 111. The W_{inter} in time region I is equal to $X_{\text{C,app}}(t)$ shown in Figure 6 which was directly determined from $I_{\text{WAXD}}^{\text{GAPP}}(q; t)$ shown in Figure 9.

Consequently, we succeeded in unequivocally verifying or confirming the conjecture given in section IV-2 concerning existence of the diffraction peaks due to the intermediate structures and its evolution prior to the evolution of the diffraction peaks due to the lamellar crystallites. We would like to stress here that the 2D-COS enables this unequivocal verification or confirmation even under the condition that the two diffraction peaks are superposed each other so that the difference in the time evolution of the two diffraction peaks are unable to be captured directly in time region II and III, as defined in Figure 8 and as shown in Figure 9b.

IV-4. MCR-ALS Analyses of WAXD Profiles. We applied the MCR-ALS analysis to decompose the net WAXD profiles into those from the intermediate structures and the lamellar crystallites in the time region II and III. The two diffraction profiles so closely overlapped each other that there are no other effective methods to decompose the observed profiles into the two diffraction profiles. Before the MCR-ALS analysis, the number of components (the number of the elemental diffraction profiles in the observed WAXD profiles in our particular case) was first determined by using the evolving factor analysis (EFA),^{34,54,55} which is outlined in the Supporting Information 2. On the basis of the EFA analyses, we determined

the two components, which will be assigned later to be the diffraction due to the intermediate structures and that due to the lamellar crystallites, for the MCR-ALS analyses of the WAXD profiles in the q regions of 9.0–10.2, 11.4–12.4, and 13.0–17.0 nm⁻¹. The results are shown in parts a, b, and c of Figure 11, respectively. Through the MCR-ALS analyses in the different q regions, we obtained the two elemental WAXD profiles, $I_{\text{inter}}(q)$ for the intermediate structures and $I_{\text{crys}}(q)$ for the lamellar crystallites, as shown by the red broken lines and blue solid lines, respectively, in the left half of Figure 11. Each of the elemental profiles is normalized in such a way that its maximum intensity is equal to 1. The time evolution of the weight fraction of the lamellar crystallites and the intermediate structures, defined as W_{crys} and W_{inter} , respectively, are plotted as a function of time with the blue and red symbols in the right half of Figure 11. The weight fractions are adjustable parameters to attain the best fit of the observed profiles $I_{\text{WAXD}}^{\text{app}}(q; t)$ with the reconstructed profiles $I_{\text{WAXD}}^{\text{recon}}(q; t)$

$$I_{\text{WAXD}}^{\text{recon}}(q; t) = W_{\text{inter}}(t)I_{\text{inter}}(q) + W_{\text{crys}}(t)I_{\text{crys}}(q) \quad (11)$$

obtained by the MCR-ALS analysis. It should be noted that $I_k(q)$ ($k = \text{inter or crys}$) is assumed to be independent of time but only $W_k(t)$ ($k = \text{inter or crys}$) changes with time in region II

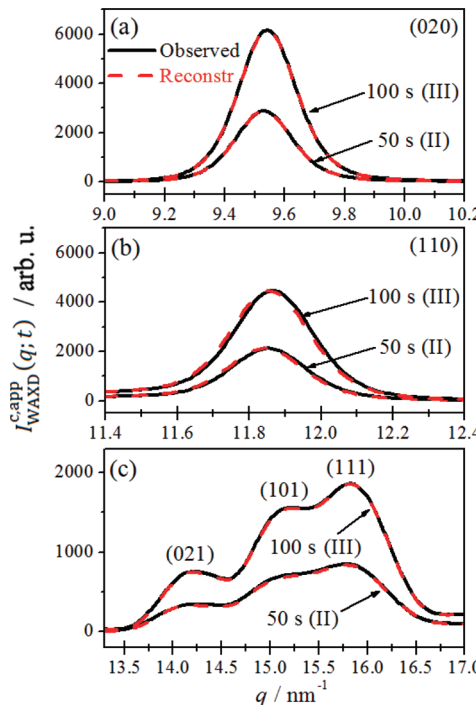


Figure 12. Comparisons of the observed WAXD profiles, $I_{\text{WAXD}}^{\text{app}}(q; t)$ (black solid lines), and the reconstructed WAXD profiles, $I_{\text{WAXD}}^{\text{recon}}(q; t)$ (red broken lines), obtained after the MCR-ALS analyses: (a) 020; (b) 110; (c) the multiple diffraction peaks composed of 021, 101, and 111.

and III. The reconstructed profiles after the MCR-ALS analyses of diffraction peaks 020 and 110 as well as the multiple diffraction peaks composed of 021, 101, and 111 at 50 and 100 s are shown in parts a, b, and c of Figure 12, respectively. A good agreement was found between the observed profiles (shown by the black solid lines) and the reconstructed profiles (shown by the red broken lines). Although it is natural to attain the good agreement, the agreement supports the validity of the MCR-ALS analysis in this work. Consequently, the WAXD profiles from the intermediate structures of PHB are clarified for the first time to be given directly by $I_{\text{WAXD}}^{\text{app}}(q; t)$ in region I and by $I_{\text{inter}}(q)$ in eq 11 together with the results show in Figure 11 in regions II and III.

Let us first discuss the normalized diffraction profiles shown in the left half of Figure 11. Comparisons between the two elemental profiles $I_{\text{inter}}(q)$ and $I_{\text{crys}}(q)$ clearly indicate that all the profiles of the former have a peak or peaks at smaller q or q' s than those of the latter, indicating that the characteristic spacings of the intermediate structures are larger than those of the lamellar crystallites, and hence the intermediate structures are less perfect than the lamellar crystallites. Moreover, in the q region of $13\text{--}17 \text{ nm}^{-1}$ shown in the left half of Figure 11c, the profile of $I_{\text{inter}}(q)$ consists of three diffraction peaks at $q = 14.0, 14.7$, and 15.5 nm^{-1} (shown by the red arrows), while that of $I_{\text{crys}}(q)$ consists of those at $14.3, 15.2$, and 15.8 nm^{-1} (shown by the blue arrows), which are almost equal to the q values where the peaks are found for the 2D asynchronous and synchronous maps in parts b and a of Figure 10, respectively. Consequently, the small q -shift in the peak positions of the diffraction profiles due to the intermediate structures is consistently found not only in the WAXD profiles themselves shown in Figure 9 but also in 2D asynchronous map shown in Figure 10b and in the elemental

profiles decomposed by MCR-ALS analyses shown in the left half of Figure 11. These results reinforce each other for unequivocal identification of existence of the intermediate structures.

Now let us discuss the variation of relative weight fractions $W_{\text{inter}}(t)$ and $W_{\text{crys}}(t)$ shown in the right half of Figure 11. They are actually evaluated in regions II and III only: The value $W_{\text{inter}}(t)$ in region I is equal to $X_{\text{capp}}(t)$: $W_{\text{inter}}(t = 32 \text{ s}) = X_{\text{capp}}(t = 32 \text{ s})$. It is found that all of the $W_{\text{inter}}(t)$ and $W_{\text{crys}}(t)$ obtained in the different q regions show the very similar trends as follows: (1) The $W_{\text{inter}}(t)$ increases from zero to a maximum value with time from 14 s (the induction time t_0) to 60 s, followed by the decrease from the maximum values to zero with a further increase of the time. Meanwhile, (2) the $W_{\text{crys}}(t)$ begins to increase from zero at around 32 s and rapidly increase with the time until 100 s, followed by the slow increase with a further increase of the time, seemingly due to the secondary crystallization process.

Thus, we can conclude that (1) only the intermediate structures grow via the transformation from the amorphous phase to the mesomorphic phase (designated as $T_{\text{am-meso}}$) after the induction time t_0 in region I, (2) both the intermediate structures and the lamellar crystallites grow via $T_{\text{am-meso}}$ and the transformation from the intermediate structures to the lamellar crystallites (designated as $T_{\text{meso-crys}}$) in region II, and (3) in region II, the rate of $T_{\text{am-meso}}$ is anticipated to be larger than that of $T_{\text{meso-crys}}$, so that W_{inter} increases with time, while in region III, the rate of $T_{\text{am-meso}}$ is anticipated to be smaller than that of $T_{\text{meso-crys}}$, so that W_{inter} decreases with time, thereby giving rise to the maximum value of W_{inter} at the boundary between II and III.

The results revealed in Figure 11 with MCR-ALS analyses are consistent with the results revealed in Figure 8 obtained by the direct observations of the WAXD profiles. The reduction of the integral widths of “apparent 020 and 110 diffraction peaks” in region I is due to the growth and ordering of the intermediate structures. The word “apparent” was used because the diffractions in this time span are from the mesomorphic orders but not from crystals. In region II, both the intermediate structures and lamellar crystallites having different spacings grow and give rise to the diffraction peaks at slightly different q 's, which accounts for the increase of the “apparent integral widths” β_{020} and β_{110} . The word “apparent” was used again because the observed diffractions comprised the two elemental profiles.

The results of MCR-ALS analyses revealed in Figure 11 provide a profound interpretation for the results shown in Figure 8c also on the time dependence of the apparent lattice spacings directly obtained from the observed WAXD profiles $I_{\text{WAXD}}^{\text{app}}(q; t)$. The apparent lattice spacings $a(t)$ and $b(t)$ in time region I reflect those from the intermediate structures only which is independent of time and larger than those from the lamellar crystallites to be developed in regions II and III. The growth of the lamellar crystallites via $T_{\text{meso-crys}}$ in regions II and III decreases $a(t)$ and $b(t)$. The results in Figures 8c and 11 are consistent and reinforce each other with respect to the concept of the multistep crystallization process via formation of the intermediate structures.

The time difference between the onsets of the intermediate mesomorphic structures and the lamellar crystallites as elucidated by MCR-ALS analyses of $W_{\text{inter}}(t)$ and $W_{\text{crys}}(t)$ in Figure 11 is consistent with that elucidated from the 2D-COS analyses shown in Figure 10 and Table 1, supporting here again the Noda's rule. The time evolution of the apparent crystallinity

$X_{C,\text{app}}(t)$ shown in Figure 6 can be analyzed more deeply by using the pieces of information on $W_{\text{crys}}(t)$ and $W_{\text{inter}}(t)$ shown in Figure 11: the apparent $X_{C,\text{app}}(t)$ can be decomposed into the true crystallinity $X_{\text{crys}}(t)$ and the weight fraction of the mesomorphic orders $X_{\text{inter}}(t)$ as follows:

$$X_{\text{crys}}(t) = \frac{X_{C,\text{app}}(t)W_{\text{crys}}(t)}{W_{\text{crys}}(t) + W_{\text{inter}}(t)} \quad (12)$$

and

$$X_{\text{inter}}(t) = X_{C,\text{app}}(t) - X_{\text{crys}}(t) \quad (13)$$

The results are also shown in Figure 6 by the blue and red symbol, respectively. $X_{\text{inter}}(t)$ increases with time from 0 at 14 s to ~10 wt % at the end of region I, to a maximum value of ~15 wt % at the end of region II, and then decreases to zero at 218 s, while $X_{\text{crys}}(t)$ increases with time from zero at the end of region I to ~12 wt % at the end of region II and to ~50 wt % at 218 s.

IV-5. Comparisons with Time-Resolved FTIR Analyses. At this stage, we shall compare the results obtained in this work with those previously obtained on the isothermal crystallization process of PHB by using the tr-FTIR methods,^{20,21} with a particular emphasis of the intermediate structures. Zhang et al.²⁰ conducted the 2D-COS analysis of the time-resolved IR bands of PHB in the $-\text{C}=\text{O}$ stretching vibration region and found the sequential changes of the characteristic bands in the order of 1743, 1731, and 1722 cm^{-1} with time. By assuming the band at 1731 cm^{-1} is due to the intermediate structures, they speculated that the sequential changes of the bands suggest transformations first from the amorphous melts to the intermediate structures and then to the lamellar crystallites with the HBs $-\text{C}=\text{O}\cdots\text{H}-\text{C}-$ between the $-\text{C}=\text{O}$ groups and one of $-\text{C}-\text{H}$ groups in $-\text{CH}_3$ along the a -axis. Suttiwijitpukdee et al.²¹ studied the time-resolved IR bands not only in the $-\text{C}=\text{O}$ stretching vibration region but also in the $-\text{C}-\text{H}$ bending and $-\text{C}-\text{O}-\text{C}$ stretching vibration regions and further elaborated such a multistep crystallization process as given by the following sequential orders: from the amorphous melts to the intermediate structures, then to the lamellar crystallites without the HBs, and finally to the lamellar crystallites with the HBs.

The present works provide a piece of solid evidence on the intermediate structures responsible for the IR band at 1731 or 1732 cm^{-1} and further elucidate the corresponding WAXD profiles (as shown by the profiles up to 32 s in Figure 9) with broad widths and the larger characteristic spacings as characterized by the results shown in region I in Figure 8 and the profiles $I_{\text{inter}}(q)$ on the left half in Figure 11 in regions II and III. The decrease of the lattice parameters $a(t)$ and $b(t)$ in regions II and III are clearly due to the formation of the well-developed lamellar crystallites in these regions. However, it is not clear yet where the HBs begin to form in the crystallization process. It may be possible to speculate the considerable amount of the HBs are formed at $t > 100$ s, beyond which $a(t)/a_\infty$ hardly changes with time and $b(t)/b_\infty$ decreases slowly with time. This time region may be the one where the secondary crystallization seems to occur as pointed out earlier in conjunction with Figure 6. Our earlier work²¹ also elucidated the HBs are formed predominantly in the secondary crystallization process. It is crucial to simultaneously investigate tr-WAXD and tr-SAXS with tr-FTIR on the same specimens in

order to further clarify the time span for the evolution of the intermediate structures and HBs, which deserves future works.

IV-6. Evolutions of High-Order Self-Assembly As Observed by SAXS Analysis. Up to this stage, we discussed the time evolution of the individual intermediate structures and crystallites from the amorphous melts. Here in this section, we shall discuss space-time organization of a higher order self-assembly (or a texture) composed of amorphous regions, intermediate structures, and crystallites in the crystallization process. The tr-SAXS profiles employed in this work enable us to explore the space-time organization of these elemental structural units in the length scale of ~50 nm.

From the one-dimensional correlation function shown in Figure 5, we determined the characteristic parameters $L(t)$, $l_c(t)$, $l_a(t)$, and $Q(t)$ as well as the local apparent crystallinity $l_c(t)/L(t)$ within the grains, which are composed of the mesomorphic layers and/or the lamellar crystallites and the intervening amorphous layers between them. The grains in turn are dispersed in the amorphous matrix. The results are shown in Figure 13 which reveal the several interesting features: (1) After

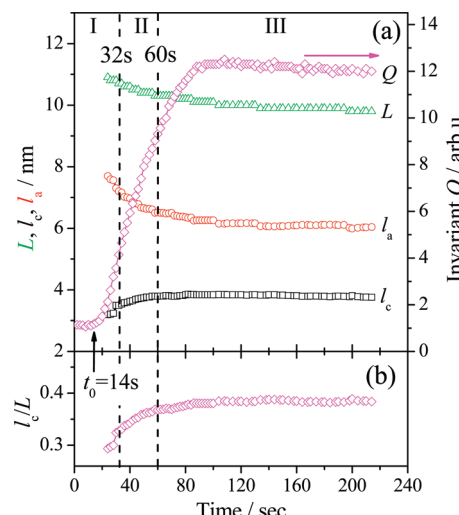


Figure 13. (a) Variations of characteristic parameters obtained from the one-dimensional correlation function such as the long period L , the mesomorphic-layer or lamellar-crystal thickness l_c , the amorphous-layer thickness l_a , and invariants Q (a) and (b) the local apparent crystallinity l_c/L as a function of time.

the induction period of $t_0 = 14$ s, the invariant Q starts to sigmoidally increase with time with an inflection point at $t \sim 60$ s as in the case of $X_{C,\text{app}}(t)$ vs t in Figure 6: it increases very rapidly in regions I and II and then slows down in region III. (2) There is only a single characteristic long spacing $L(t)$ evolved throughout the whole crystallization process, and the spacing slightly decreases with time at a relatively larger rate in regions I and II than in region III and reaches an almost constant value at $t > 100$ s in region III (seemingly in the secondary crystallization regime). (3) There is only a single thickness l_c of either the layers composed of the intermediate structures or the lamellar crystallites which continuously increases slightly with time throughout the whole crystallization process at a largest rate in region I, followed by the decreasing rate in the order of regions II and III, and eventually reaches a constant value at $t > 100$ s. (4) The value $l_a(t)$ decreases more largely with time as a consequence of the increasing $l_c(t)$ and decreasing $L(t)$.

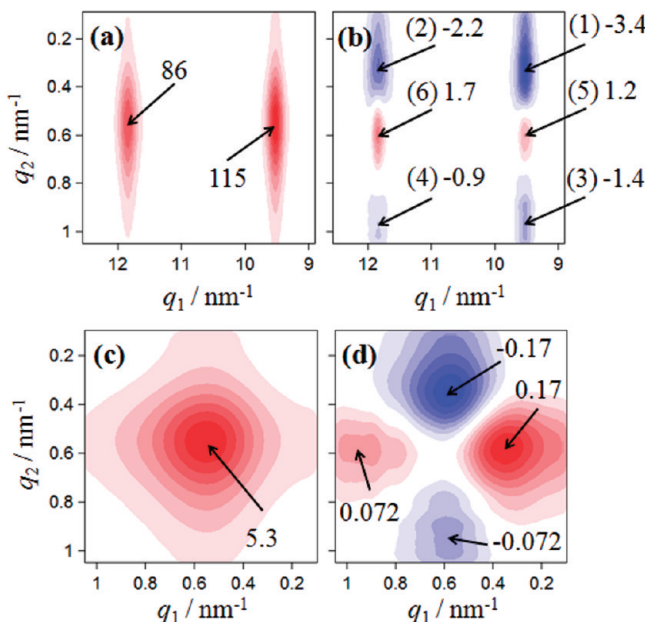


Figure 14. 2D-COS between the tr-WAXD and tr-SAXS profiles in region I from 16 to 32 s: (a) synchronous map $\Phi(q_1, q_2)$ and (b) asynchronous map $\Psi(q_1, q_2)$; and the 2D-COS between the tr-SAXS profiles themselves: (c) synchronous map $\Phi(q_1, q_2)$ and (d) asynchronous map $\Psi(q_1, q_2)$. The red and blue areas indicate the positive and negative correlation intensities, respectively. The number attached to each arrow indicates the maximum or minimum intensity of the positive or negative correlation peak, respectively.

Evidence (2) and (3) described above reveal themselves that the intermediate structures developed in region I grow into the layers with mesomorphic orders (defined as layers or mesomorphic layers) periodically arranged in space with amorphous melt layers intervening between them and that the mesomorphic layers are continuously transformed into the lamellar crystallites in regions II and III. The small decreases of L [evidence (2)] may be interpreted as a consequence of insertions of new mesomorphic layers or lamellar crystallites in the space between the as-grown mesomorphic layers or lamellar crystallites (“car-parking problems” in fixed parking area).^{1,24,25} In region I, only the mesomorphic layers grow, and its thickness $l_c(t)$ increases with t , implying that the chains in the layers tend to have more stretched conformations (helical conformations) with increasing degree of mesomorphic orders compared with random-coil conformations in the melt. The $l_c(t)$ further increases in region II to reach the critical thickness, followed by the transformation from the mesomorphic layers to the lamellar crystallites as proposed by Strobl.²⁹ This means that the chains tend to have even more stretched conformation accompanied by the transformation. We will present a schematic illustration for the assembly of the mesomorphic layers, the lamellar crystallites, and the amorphous layers formed in the crystallization process in Figure 15 in section V.

IV-7. 2D Correlation Analyses between SAXS and WAXD Profiles. Since the SAXS and WAXD profiles were collected simultaneously, they can be used to analyze the time sequence on the evolution of these two profiles by means of the heterospectral 2D-COS analysis between the Lorentz-corrected SAXS profiles $q^2 I_{\text{SAXS,C}}(q; t)$ and the WAXD profiles $I_{\text{WAXD}}^{\text{app}}(q; t)$ corrected for the amorphous halo. We have already clarified from the 2D-COS analysis (IV-3) and MCR-ALS analysis (IV-4) of the tr-WAXD profiles that only the intermediate

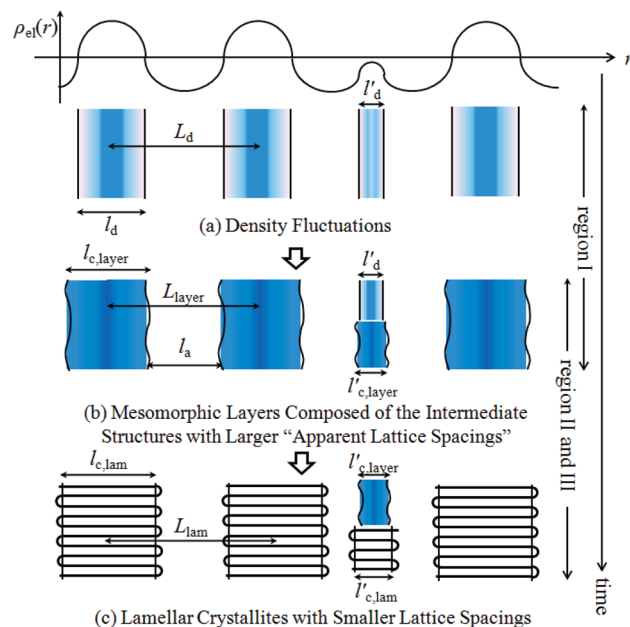


Figure 15. Schematic illustration of the multistep crystallization process involving the continuous transformation of first (a) the density-rich regions to (b) the mesomorphic layers and then from the mesomorphic layers to (c) the lamellar crystallites, which involves also the continuous increase of the size of the fundamental structural units from l_d to $l_{c,\text{layer}}$ and from $l_{c,\text{layer}}$ to $l_{c,\text{lam}}$.

structures form in region I; both the intermediate structures and the lamellar crystallites grow in region II. Consequently, in this section we will focus on the 2D-COS analysis between $q^2 I_{\text{SAXS,C}}(q; t)$ and $I_{\text{WAXD}}^{\text{app}}(q; t)$ in time region I (from 16 to 32 s) in order to confirm the evolution of the intermediate structures with respect to tr-SAXS in this time region.

As shown in Figure 4b, $q^2 I_{\text{SAXS,C}}(q; t)$ from 16 to 32 s shows the shift of the peak position from $q = 0.50$ to 0.55 nm^{-1} . One may worry about the effect of this peak shift on the 2D-COS analysis. However, we believe that this shift $\sim 10\%$ is small enough so that it will not cause any serious errors. We confirmed this fact by taking 2D-COS with the reduced SAXS profiles $I_{\text{SAXS,C}}(q/q_{\max}; t)$, where q is reduced by the time-dependent peak position $q_{\max}(t)$ so that the reduced SAXS profiles do not show the peak shift (see Figures S4-1 and S4-2 in Supporting Information 4).

Figures 14a and 14b show the synchronous $\Phi(q_1, q_2)$ and asynchronous $\Psi(q_1, q_2)$ 2D correlation maps obtained during the isothermal crystallization process from 16 to 32 s (in region I), respectively. The red and blue areas indicate the regions with the positive and negative correlation intensities, respectively. In the synchronous map (part a), there are two positive peaks: $\Phi(9.5, 0.6) > 0$ and $\Phi(11.9, 0.6) > 0$, while in the asynchronous map (part b), there are two strongly negative peaks: (1) $\Psi(9.5, 0.36) < 0$ and (2) $\Psi(11.9, 0.36) < 0$, two weakly negative peaks: (3) $\Psi(9.5, 0.97) < 0$ and (4) $\Psi(11.9, 0.97) < 0$, and two weakly positive peaks: (5) $\Psi(9.5, 0.6) > 0$ and (6) $\Psi(11.9, 0.6) > 0$. If the time evolution of the SAXS peak around $q = 0.6 \text{ nm}^{-1}$ and those of the 020 WAXD peak around $q = 9.5 \text{ nm}^{-1}$ and the 110 WAXD peak around $q = 11.9 \text{ nm}^{-1}$ have the common time evolution process, involving only formation of the intermediate structures, we will not be able to observe the cross-peaks in the asynchronous map as shown in Figure 14b. Existence of the asynchronous cross-peaks thereby implies clearly a piece of solid evidence that there

must be at least another component, which influences the time-evolution of the SAXS profiles at a different rate, in addition to the evolution of the intermediate structures as observed by the WAXD profiles, although the time evolution of the SAXS profiles (Figures 4b and 13) and that of WAXD profiles (Figures 6 and 9) are very similar, and thereby they do not suggest directly existence of the another component.

Let us first take a look at the 2D-COS and find out a possible additional component. The negative asynchronous peaks labeled by (1) to (4) in Figure 14b together with the positive synchronous correlation intensities at the respective peak positions shown in Figure 14a suggest such a sequential order as follows: The SAXS intensities at $q = 0.36$ and 0.97 nm^{-1} evolve faster than the WAXD peak intensities at $q = 9.5$ and 11.9 nm^{-1} [defined hereafter as sequential order (1)], if the Noda's rule is applicable to the 2D-COS between tr-SAXS and tr-WAXD profiles. Let us next consider below if there are any plausible models to explain the above sequential order (1) attained by this rule. We conjecture that the additional component described above must be the density fluctuations which are built up in the homogeneous amorphous matrix prior to the formation of the intermediate structures. The mesomorphic layers composed of the intermediate structures, which are periodically developed in space, give rise to $I_{\text{SAXS}}^{\text{interm}}(q; t)$ with a peak at $q \sim 0.6 \text{ nm}^{-1}$. The density fluctuations give rise to $I_{\text{SAXS}}^{\text{density}}(q; t)$ which has an intensity distribution with q much broader than $I_{\text{SAXS}}^{\text{interm}}(q; t)$, so that the observed intensity at $q \sim 0.6 \text{ nm}^{-1}$ is dominated by $I_{\text{SAXS}}^{\text{interm}}(q; t)$ but that at $q \sim 0.36$ or 0.97 nm^{-1} is dominated by $I_{\text{SAXS}}^{\text{density}}(q; t)$. Under this condition if the density fluctuations evolve faster than the periodic mesomorphic layers, the sequential order (1) found above can be accounted for. Thus, this sequential order (1) is unveiled only by the precise analysis of the 2D-COS.

Let us next consider the asynchronous peaks (5) $\Psi(9.5, 0.6)$ and (6) $\Psi(11.9, 0.6)$ in Figure 14b having a weak positive intensity. The small absolute intensity of these two asynchronous peaks compared with the large absolute intensity of the asynchronous peaks (1) and (2) must imply that the evolution of the peaks at $q = 0.6$ and 9.5 or 11.9 nm^{-1} is less asynchronous (or more synchronous) than the evolution of the peaks at $q = 0.36$ and 9.5 or 11.9 nm^{-1} . The small positive intensity of the asynchronous peak (5) and peak (6) together with the positive synchronous intensity at the respective positions imply such a sequential order as follows: The WAXD intensities at $q = 9.5$ and 11.9 nm^{-1} evolve slightly faster than the evolution of the SAXS peak at $q = 0.6 \text{ nm}^{-1}$ according to the Noda's rule [defined hereafter as sequential order (2)]. This sequential order may infer that the intermediate structures first locally developed in the as-formed density-rich region [stage (i)]; then the locally developed intermediate structures grow and order into the mesomorphic layers composed of the intermediate structures [stage (ii)]. Consequently, this sequential order (2) occurs after the sequential order (1). One should note that the WAXD peaks at $q = 9.5$ and 11.9 nm^{-1} are sensitive to the locally developed intermediate structures, while the SAXS peak at $q = 0.6 \text{ nm}^{-1}$ is sensitive to the periodic mesomorphic layers. In stage (i), the SAXS peak due to the density fluctuations may not exist or even if it exists, it may not be remarkable at least, thereby satisfying the condition of $I_{\text{SAXS}}^{\text{density}}(q = 0.6 \text{ nm}^{-1}; t) < I_{\text{SAXS}}^{\text{interm}}(q = 0.6 \text{ nm}^{-1}; t)$, while in stage (ii) the SAXS peak due to the periodic mesomorphic layers must be increasingly remarkable with time. Thus, we would like to stress that this information also is unveiled only by the precise

analysis of the 2D-COS but cannot be ever obtained at all by the direct comparisons of the tr-SAXS and the tr-WAXD. Consequently, the Noda's rule applied to the 2D-COS between the tr-SAXS and tr-WAXD profiles seems to provide a physically reasonable model.

On the basis of this heterospectral 2D-COS analysis described above together with the previous FTIR results,²¹ we propose that the density fluctuations are first formed in the homogeneous melts; then the density-rich regions locally develop the intermediate structures with the mesomorphic orders. Upon a further elapse of time, the locally developed intermediate structures grow into the mesomorphic layers; the mesomorphic layers are then transformed first into the lamellar crystallites without HBs and eventually those with HBs.

IV-8. 2D Correlation Analyses between SAXS Profiles. If the time changes in the SAXS profiles in region I are composed of $I_{\text{SAXS}}^{\text{density}}(q; t)$ and $I_{\text{SAXS}}^{\text{interm}}(q; t)$ which evolve at different rates as elucidated in section IV-7, the 2D-COS of tr-SAXS profiles themselves taken in region I are expected to give rise to the asynchronous 2D cross-peaks. Figures 14c and 14d show the synchronous and asynchronous 2D correlation maps, $\Phi(q_1, q_2)$ and $\Psi(q_1, q_2)$, respectively, taken from the Lorentz-corrected SAXS profiles from 16 to 32 s (corresponding to region I only). The red and blue areas indicate the positive and negative correlation intensities, respectively. The data shows that $\Phi(0.6, 0.36) > 0$ and $\Psi(0.6, 0.36) < 0$; $\Phi(0.97, 0.6) > 0$ and $\Psi(0.97, 0.6) > 0$, implying such a sequential order as the intensity at $q = 0.36$ and 0.97 nm^{-1} changing faster than the intensity at $q = 0.6 \text{ nm}^{-1}$ according to the Noda's rule. This suggests that the density fluctuations are built up faster than formation of the mesomorphic layers. This result seems to be reasonable and is consistent with the results obtained in section IV-7, thereby supporting the Noda's rule. We would like to stress again that this conclusion is obtained by the 2D-COS analysis only but not by the direct observations of the tr-SAXS results shown in Figures 4b and 13.

V. CONCLUSION

The multistep crystallization process as revealed by tr-SAXS and tr-WAXD investigations of PHB is partially presented by schematic illustration shown in Figure 15. The density fluctuations are first built up in the molten bulk PHB (a), density-rich regions are then transformed into the layers composed of the intermediate structures with the mesomorphic orders between the melts and well-developed lamellar crystallites (b), and the mesomorphic layers are eventually transformed into the well-ordered lamellar crystallites (c). We think that the structural transformation process from (b) to (c) may involve the process proposed by Strobl (see Figures 1 and 2 of ref 29): a spontaneous thickening of the mesomorphic layer up to a critical value, followed by the transformation into a granular crystalline layer, and finally the transformation into homogeneous lamellar crystallites. Our work captures the trend of these detail processes in the process from (b) to (c), as already discussed in the last part of the last paragraph in section IV-6 in conjunction with increasing $I_c(t)$ in regions I and II. We believe that our model is consistent with the Strobl's model and further reinforce it by adding new pieces of evidence as summarized below.

The transformation from (a) to (b) occurs in time region I, which was clarified by (1) 2D-COS between tr-SAXS and tr-WAXD profiles (section IV-7, Figure 14a,b) and (2) 2D-COS of tr-SAXS profiles themselves (section IV-8, Figure 14c,d).

The transformation from (b) to (c) occurs in time region II and III, which was clarified by (3) the precise analysis of the integral widths (section IV-2, Figure 8), (4) the 2D-COS of the tr-WAXD profiles (section IV-3, Figure 10), (5) the MCR-ALS of the tr-WAXD profiles (section IV-4, Figure 11), and (6) the conventional one-dimensional correlation function analysis of tr-SAXS profiles (section IV-6, Figure 13). The analysis (1) elucidates that the density fluctuations are first built up in a homogeneous amorphous melt; then the density-rich regions locally develop the intermediate structures with the mesomorphic orders; the locally developed intermediate structures grow into the layer with the long spacing. The analysis (5) further distinguishes region II and III as follows: in region II, relative weight fractions of both the intermediate structures comprising the mesomorphic orders (W_{inter}) and the well-developed lamellar crystallites (W_{crys}) increase with time; while in region III, W_{inter} decreases and W_{crys} increases with time. The difference in the time dependence of W_{inter} and W_{crys} in regions II and III is attributed to the difference in transformation rate from (a) to (b) ($T_{\text{am-meso}}$) and from (b) to (c) ($T_{\text{meso-crys}}$) in these two regions: the rate $T_{\text{am-meso}} >$ the rate $T_{\text{meso-crys}}$ in region II and opposite is the case in region III, as discussed in section IV-4. The analysis (5) identified the diffraction profiles from the intermediate structures and well-developed lamellar crystallites in regions II and III, while the diffraction profiles from the intermediate structures in region I was directly identified by the analysis (3). The analyses (3) to (5) elucidated that the “apparent lattice spacings” of the intermediate structures are larger than the lattice spacings of the lamellar crystallites.

The analysis (6) elucidated the time evolution of the characteristic parameters such as the scattering invariant $Q(t)$, the long spacing $L(t)$ of the mesomorphic layers [$L_{\text{layer}}(t)$] and/or the lamellar crystallites [$L_{\text{lam}}(t)$], the thickness $l_c(t)$ of the mesomorphic layers [$l_{c,\text{layer}}(t)$] and/or the lamellar crystallites [$l_{c,\text{lam}}(t)$], and the local volume fraction of the mesomorphic layers or the lamellar crystallites within their grains, $l_c(t)/L(t)$, which are dispersed in the matrix of the amorphous melts (see Figure 15). The results shown in Figure 13 revealed that the mesomorphic layers are continuously transformed into the lamellar crystallites, giving rise to continuous variations of $L(t)$ from $L_{\text{layer}}(t)$ to $L_{\text{lam}}(t)$ and $l_c(t)$ from $l_{c,\text{layer}}(t)$ to $l_{c,\text{lam}}(t)$ with time.

The small decrease of $L(t)$ with t may be due to the evolution of new density-rich regions with thickness l_d' and their transformations first into the mesomorphic layers and then to lamellar crystallites with the thicknesses $l_{c,\text{layer}}'(t)$ and $l_{c,\text{lam}}'(t)$, respectively, in the amorphous regions between the as-developed density-rich regions, layers, or crystallites, as illustrated in the third column of Figure 15a–c. The thickness l_d' , $l_{c,\text{layer}}'$, and $l_{c,\text{lam}}'$ may be smaller than l_d , $l_{c,\text{layer}}$, and $l_{c,\text{lam}}$, respectively, in the case when the thickness $l_a(t)$ is not sufficiently large for the newly inserted density-rich regions, layers, and/or crystallites. The density-rich regions with l_d' in part (a) are expected to increase its density to a sufficiently high level before they are transformed into the mesomorphic layers with $l_{c,\text{layer}}'$ as illustrated in part (b).

The increase of $l_c(t)$ and $l_c(t)/L(t)$ was discussed in section IV-6. The transformation from (a) to (b) must involve a change in the single chain conformations from more or less random coil conformations to the stretched chain conformations (or increasing fraction of helical conformations) in order for the chains to be incorporated in the mesomorphic orders. This may

involves an increase of the thickness in the density-rich regions from l_d (or l_d') to the thickness of the mesomorphic layers $l_{c,\text{layer}}$ (or $l_{c,\text{layer}}'$), while the characteristic spacing for the density fluctuations L_d may be almost the same as L_{layer} .

Finally, we would like to stress that the conclusions achieved in this work solidify those reported by the earlier works and strengthen the universal features of the multistep crystallization process for bulk polymer melts. We would like to remark also the point that the isothermal crystallization at the same temperature from glassy states is quite intriguing in comparison with that from melts. This deserves future works.

ASSOCIATED CONTENT

Supporting Information

(1) One-dimensional correlation function analysis; (2) MCR-ALS and EFA algorithm and their results; (3) Avrami plots on $X_{\text{C,app}}(t)$ and $X_{\text{crys}}(t)$; (4) heterospectral and homospectral 2D-COS analyses with tr-SAXS profiles and their results. This material is available free of charge via the Internet at <http://pubs.acs.org>.

AUTHOR INFORMATION

Corresponding Author

*E-mail: ozaki@kwansei.ac.jp (Y.O.); hsato@kwansei.ac.jp (H.S.).

ACKNOWLEDGMENTS

This work was supported by Grant-in-Aid for Scientific Research (C) from MEXT (No. 20550026, No. 20550197), Grant-in-Aid for Scientific Research on Innovative Areas from MEXT (No. 21106521), and Shiseido Female Researcher Science Grant 2009. This work was supported also by Kwansei-Gakuin University “Special Research” project 2009–2014. The authors thank beam time during experiments at Frontier Softmaterial Beamline: FSBL 03XU in SPring-8.

REFERENCES

- (1) Strobl, G. R. *The Physics of Polymers*; Springer-Verlag: Berlin, 1997.
- (2) Lotz, B. *Eur. Phys. J. E* **2000**, *3*, 185–1894.
- (3) Wunderlich, B. *Prog. Polym. Sci.* **2003**, *28*, 383–450.
- (4) Cornibert, J.; Marchessault, R. H. *J. Mol. Biol.* **1972**, *71*, 735–756.
- (5) Yokouchi, M.; Chatani, Y.; Tadokoro, H.; Teranishi, K.; Tani, H. *Polymer* **1973**, *14*, 267–272.
- (6) Doi, Y. *Microbial Polyester*; VCH Publishers: New York, 1990.
- (7) Anderson, A. J.; Dawes, E. A. *Microbiol. Rev.* **1990**, *54*, 450–472.
- (8) Lara, M. L.; Gjalt, H. W. *Microbiol. Mol. Biol. Rev.* **1999**, *63*, 21–53.
- (9) Iwata, T.; Doi, Y. *Macromol. Chem. Phys.* **1999**, *200*, 2429–2442.
- (10) Sato, H.; Nakamura, M.; Padermshoke, A.; Yamaguchi, H.; Terauchi, H.; Ekgasit, S.; Noda, I.; Ozaki, Y. *Macromolecules* **2004**, *37*, 3763–3769.
- (11) Sato, H.; Murakami, R.; Padermshoke, A.; Hirose, F.; Senda, K.; Noda, I.; Ozaki, Y. *Macromolecules* **2004**, *37*, 7203–7213.
- (12) Sato, H.; Murakami, R.; Zhang, J.; Mori, K.; Takahashi, I.; Terauchi, H.; Noda, I.; Ozaki, Y. *Macromol. Symp.* **2005**, *230*, 158–166.
- (13) Sato, H.; Mori, K.; Murakami, R.; Ando, Y.; Takahashi, I.; Zhang, J.; Terauchi, H.; Hirose, F.; Senda, K.; Tashiro, K.; Noda, I.; Ozaki, Y. *Macromolecules* **2006**, *39*, 1525–1531.
- (14) Sato, H.; Ando, Y.; Dybal, J.; Iwata, T.; Noda, I.; Ozaki, Y. *Macromolecules* **2008**, *41*, 4305–4312.
- (15) Guo, L. H.; Sato, H.; Hashimoto, T.; Ozaki, Y. *Macromolecules* **2010**, *43*, 3897–3902.
- (16) Guo, L. H.; Sato, H.; Hashimoto, T.; Ozaki, Y. *Macromolecules* **2011**, *44*, 2229–2239.

- (17) Suttiwijitpukdee, N.; Sato, H.; Zhang, J.; Hashimoto, T.; Ozaki, Y. *Polymer* **2011**, *52*, 461–471.
- (18) An, Y.; Dong, L.; Li, L.; Mo, Z.; Feng, Z. *Eur. Polym. J.* **1999**, *35*, 365–369.
- (19) Androsch, R. *Polymer* **2008**, *49*, 4673–4679.
- (20) Zhang, J.; Sato, H.; Noda, I.; Ozaki, Y. *Macromolecules* **2005**, *38*, 4274–4281.
- (21) Suttiwijitpukdee, N.; Sato, H.; Zhang, J.; Hashimoto, T. *Macromolecules* **2011**, *44*, 3467–3477.
- (22) Tashiro, K.; Sasaki, S.; Gose, N.; Kobayashi, M. *Polym. J.* **1998**, *30*, 485–491.
- (23) Kanig, G. *Colloid Polym. Sci.* **1991**, *269*, 1118–1125.
- (24) Saito, K.; Hashimoto, T. *Mater. Res. Soc. Symp. Proc.* **1986**, *79*, 267–276.
- (25) Saito, K.; Zhu, Y. P.; Hashimoto, T.; Wasiak, A.; Brzostowski, N. *J. Appl. Polym. Sci.* **2007**, *105*, 137–157.
- (26) Okada, T.; Saito, H.; Inoue, T. *Macromolecules* **1992**, *25*, 1908–1911.
- (27) Pogodina, N. V.; Siddiquee, S. K.; van Egmond, J. W.; Winter, H. H. *Macromolecules* **1999**, *32*, 1167–1174.
- (28) Matsuba, G.; Kaji, K.; Nishida, K.; Kanaya, T.; Imai, M. *Polym. J.* **1999**, *31*, 722–727.
- (29) Strobl, G. R. *Eur. Phys. J. E* **2000**, *3*, 165–183.
- (30) Sajkiewicz, P.; Hashimoto, T.; Saito, K.; Gradys, A. *Polymer* **2005**, *46*, 513–521.
- (31) Noda, I. *Appl. Spectrosc.* **1993**, *47*, 1329–1336.
- (32) Noda, I.; Dowrey, A. E.; Marott, C.; Story, G. M.; Ozaki, Y. *Appl. Spectrosc.* **2000**, *54*, 236A–248A.
- (33) Noda, I.; Ozaki, Y. *Two-Dimensional Correlation Spectroscopy*; John Wiley & Sons: Chichester, UK, 2004.
- (34) Marquez-Alvarez, C.; Rodriguez-Ramos, I.; Guerrero-Ruiz, A.; Haller, G. L.; Fernandez-Garcia, M. *J. Am. Chem. Soc.* **1997**, *119*, 2905–2914.
- (35) Larrechi, S. M.; Rius, X. F. *Appl. Spectrosc.* **2004**, *58*, 47–53.
- (36) Garrido, M.; Lazaro, I.; Larrechi, S. M.; Rius, X. F. *Anal. Chim. Acta* **2004**, *515*, 65–73.
- (37) Spegazzini, N.; Ruisánchez, I.; Larrechi, S. M.; Cadiz, V.; Canadell, J. *Analyst* **2008**, *133*, 1028–1035.
- (38) Perera, P.; Wyche, M.; Loethen, Y.; Ben-Amotz, D. *J. Am. Chem. Soc.* **2008**, *130*, 4576–4577.
- (39) Spegazzini, N.; Ruisánchez, I.; Larrechi, S. M. *Anal. Chim. Acta* **2009**, *642*, 155–162.
- (40) Blobel, J.; Bernado, P.; Svergun, I. D.; Tauler, R.; Pons, M. *J. Am. Chem. Soc.* **2009**, *131*, 4378–4386.
- (41) Iglesias-Juez, A.; Kubacka, A.; Fernandez-Garcia, M.; Michiel, M. D.; Newton, M. A. *J. Am. Chem. Soc.* **2011**, *133*, 4484–4489.
- (42) Sasaki, S.; Sato, H.; Funatsu, R.; Yoshimoto, J.; Masunaga, H.; Ogawa, H. *SPring-8 User Experiment Report 2008B*, 2026. Masunaga, H.; Ogawa, H.; Sasaki, S. *SPring-8 User Experiment Report 2010B*, 1068.
- (43) Strobl, G. R.; Schneider, M. *J. Polym. Sci., Polym. Phys. Ed.* **1980**, *18*, 1343–1359.
- (44) Guinier, A. *Ann. Phys.* **1939**, *12*, 161–237.
- (45) Guinier, A.; Fournet, G. *Small Angle X-ray Scattering*; John Wiley & Sons, Inc.: London, 1955.
- (46) Porod, G. *Kolloidn. Zh.* **1951**, *124*, 83–111.
- (47) Porod, G. *Kolloidn. Zh.* **1952**, *125*, 51–57.
- (48) The integral of $[I(q)q^2]$ in the equation means the integration of the relevant diffraction peak intensity (with the spherically symmetric distribution for the powder patterns) overall reciprocal space. For systems having a spherically symmetric diffraction intensity distribution in the reciprocal space, this definition of the integral width is physically more reasonable than the conventional definition of $\beta = [\text{integral of } I(q)]/I_{\max}(q)$.
- (49) Hsiao, B. S.; Wang, Z.; Yeh, F.; Gao, Y.; Sheth, C. K. *Polymer* **1999**, *40*, 3515–3523.
- (50) Sasaki, S.; Tashiro, K.; Kobayashi, M.; Izumi, Y.; Kobayashi, K. *Polymer* **1999**, *40*, 7125–7135.
- (51) Lisowski, S. M.; Liu, Q.; Cho, J.; Runt, J.; Yeh, F.; Hsiao, B. S. *Macromolecules* **2000**, *33*, 4842–4849.
- (52) Hama, H.; Tashiro, K. *Polymer* **2003**, *44*, 6973–6988.
- (53) Reddy, R. K.; Tashiro, K.; Sakurai, T.; Yamaguchi, N.; Sasaki, S.; Masunaga, H.; Takata, M. *Macromolecules* **2009**, *42*, 4191–4199.
- (54) Maeder, M. *Anal. Chem.* **1987**, *59*, 527–530.
- (55) Il'ichev, Y. V.; Schworer, M. A.; Wirz, J. *J. Am. Chem. Soc.* **2004**, *126*, 4581–4595.